Annu. Rev. Mater. Res. 2005. 35:539–69
doi: 10.1146/annurev.matsci.35.102103.090513
Copyright © 2005 by Annual Reviews. All rights reserved
First published online as a Review in Advance on April 1, 2005

MATERIALS CHARACTERIZATION IN THE ABERRATION-CORRECTED SCANNING TRANSMISSION ELECTRON MICROSCOPE

M. Varela,[1] A.R. Lupini,[1] K. van Benthem,[1] A.Y. Borisevich,[1] M.F. Chisholm,[1] N. Shibata,[2] E. Abe,[3] and S.J. Pennycook[1]

[1]*Oak Ridge National Laboratory, Condensed Matter Science Division, Oak Ridge, Tennessee, 37831; email: mvarela@ornl.gov, arl1000@ornl.gov, Benthem@ornl.gov, albinab@ornl.gov, chisholmmf@ornl.gov, pennycooksj@ornl.gov*

[2]*Institute of Engineering Innovation. University of Tokyo, Tokyo 113-8656 Japan; email: shibata@sigma.t.u-tokyo.ac.jp*

[3]*Dept. of Materials Engineering, University of Tokyo, 7-3-1 Hongo, Bunkyo-ku, Tokyo 113-8656; email: abe@material.t.u-tokyo.ac.jp*

Key Words *Z*-contrast microscopy, electron energy loss spectroscopy, nanotechnology, complex oxides, catalysis, semiconductors

■ **Abstract** In the nanoscience era, the properties of many exciting new materials and devices will depend on the details of their composition down to the level of single atoms. Thus the characterization of the structure and electronic properties of matter at the atomic scale is becoming ever more vital for economic and technological as well as for scientific reasons. The combination of atomic-resolution *Z*-contrast scanning transmission electron microscopy (STEM) and electron energy loss spectroscopy (EELS) represents a powerful method to link the atomic and electronic structure to macroscopic properties, allowing materials, nanoscale systems, and interfaces to be probed in unprecedented detail. *Z*-contrast STEM uses electrons that have been scattered to large angles for imaging. The relative intensity of each atomic column is roughly proportional to Z^2, where Z is the atomic number.Recent developments in correcting the aberrations of the lenses in the electron microscope have pushed the achievable spatial resolution and the sensitivity for imaging and spectroscopy in the STEM into the sub-Ångstrom (sub-Å) regime, providing a new level of insight into the structure/property relations of complex materials. Images acquired with an aberration-corrected instrument show greatly improved contrast. The signal-to-noise ratio is sufficiently high to allow sensitivity even to single atoms in both imaging and spectroscopy. This is a key achievement because the detection and measurement of the response of individual atoms has become a challenging issue to provide new insight into many fields, such as catalysis, ceramic materials, complex oxide interfaces, or grain boundaries. In this article, the state-of-the-art for the characterization of all of these

Annu. Rev. Mater. Res. 0.0:${article.fPage}-${article.lPage}. Downloaded from arjournals.annualreviews.org
by Oak Ridge National Lab on 06/06/05. For personal use only.

different types of materials by means of aberration-corrected STEM and EELS are reviewed.

INTRODUCTION

The characterization of structure and electronic properties of materials at the atomic scale is a key issue for nanotechnology and many other fields of materials science. Transmission electron microscopy (TEM) techniques are so far one of the most useful for structure characterization at the atomic scale. At present, the TEM field is undergoing major, revolutionary changes thanks to the introduction of aberration correction. As a result, the sub-Å regime has been successfully achieved in the STEM, which as of today holds the record in spatial resolution for a direct image of a crystal lattice (1). More importantly, the combination of atomic-resolution *Z*-contrast STEM and EELS represents a powerful method to link the atomic and electronic structure of solids to their macroscopic properties (2–6), which allows the properties of materials, nanoscale systems, and interfaces to be probed in unprecedented detail. The detection and measurement of the response of individual atoms has become a challenging issue to provide new insight into many fields, as distributions of isolated atoms deeply modify the physical properties of many of the technologically most relevant and scientifically most interesting materials. Therefore, the possibility of identifying, localizing, and even measuring the electronic properties of single atoms represents the ultimate advance for understanding the atomic origins of materials properties.

In the first section we review the state-of-the-art in characterization of materials and nanostructures by means of aberration-corrected STEM and EELS. As many different systems are dealt with, we intend to show some of the most representative examples published so far, ranging from catalysts to semiconductors and several complex oxides. In the second section we discuss aberration correction, which has allowed direct imaging of a crystal lattice at sub-Å resolution and the routine imaging of single atoms. This part is technical in nature, so readers interested purely in materials characterization per se can move directly to the third section, in which the most recent advances in the application of STEM to a number of materials are reviewed. We present a few examples to show the tremendous impact of STEM developments in catalysis and also in ceramic materials science. The next subsections review the latest applications of STEM-EELS to the characterization of complex metallic alloys and oxides, enabling the possibility of single-atom spectroscopic detection and including the most recent accomplishments in light atom detection. The most recent structural and electronic characterization of several heterophase interfaces are described. Finally, we deal with the possibilities of three-dimensional depth slicing, an unexpected benefit of aberration correction that may finally overcome projection problem that microscopy has suffered from for the past 70 years.

Annu. Rev. Mater. Res. 0.0:${article.fPage}-${article.lPage}. Downloaded from arjournals.annualreviews.org
by Oak Ridge National Lab on 06/06/05. For personal use only.

1 Apr 2005 20:51 AR AR246-MR35-17.tex XMLPublishSM(2004/02/24) P1: KUV
AR REVIEWS IN ADVANCE10.1146/annurev.matsci.35.102103.090513

ABERRATION CORRECTION IN THE SCANNING TRANSMISSION ELECTRON MICROSCOPE

Achieving sub-Å resolution has been one of the main goals of advanced electron microscopy in order to allow atomic resolution characterization of a variety of materials. However, the spatial resolution is limited by the lens aberrations. In the 21st century, the promise of aberration correction has finally turned into a reality. For the first time, a direct image of a crystal lattice with sub-Å resolution was acquired by Nellist et al. in a dedicated VG Microscopes HB 603 U_STEM equipped with a Nion aberration corrector (1).

Although there are several excellent reviews on how the STEM works (7–9), we focus here on describing the basics of aberration correction in the STEM and how it has created a unique structural and electronic probe to study the most fascinating materials science problems.

A schematic of a STEM is shown in Figure 1. The essential difference between the optics of a STEM and a conventional transmission electron microscope

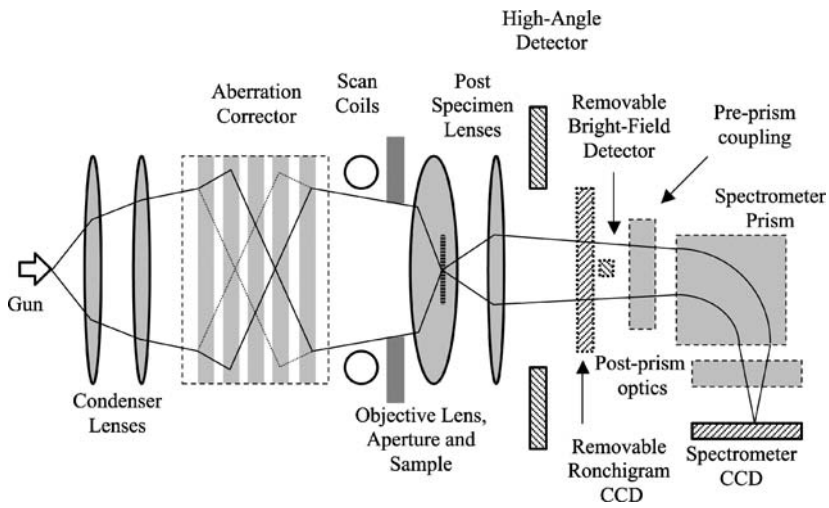

Figure 1 Simplified schematic of an aberration-corrected STEM; examples of electron trajectories are indicated. In the (quadrupole-octupole) aberration corrector, the different trajectories in the XZ and YZ planes are indicated with dotted and solid lines, respectively. The electrons are accelerated from the gun; condenser lenses are used to adjust the beam current and beam coherence and to couple to the aberration corrector. The objective lens focuses the probe, which is scanned across the sample by the scan coils. The high-angle detector collects electrons scattered to high angles. Removable bright field and Ronchigram detectors are shown as well as the important components of the spectrometer.

Annu. Rev. Mater. Res. 0.0:${article.fPage}-${article.lPage}. Downloaded from arjournals.annualreviews.org
by Oak Ridge National Lab on 06/06/05. For personal use only.

Annu. Rev. Mater. Res. 0.0:${article.fPage}-${article.lPage}. Downloaded from arjournals.annualreviews.org
by Oak Ridge National Lab on 06/06/05. For personal use only.

(CTEM) is that for a CTEM, a large area of the sample is illuminated and the significant magnification is performed by the lens system after the specimen, allowing the whole image to be recorded at once. In a STEM, the focusing is done before the electrons reach the specimen to form a very tiny probe (of the order of 1 Å), which is scanned over the sample (10). The scattered electrons are then collected in order to form the image as a function of position. In practice, a STEM will also have a series of condenser lenses that allow the beam current and coherence to be varied. Postspecimen lenses allow the detector angles to be changed.

One advantage of a STEM is that a variety of detectors can be used simultaneously. For example, it is possible to record both low- and high-angle-scattered electrons, as well as those on axis, which can be used to form a bright field (BF) image. The principle of reciprocity (10) shows that the BF STEM image should be equivalent to a CTEM image recorded under equivalent conditions. Electrons at other angles can be used to acquire several BF images at different tilts simultaneously, thus allowing schemes such as super-resolution (11). Other useful signals include back-scattered and secondary electrons, photon emission (including X-rays), and the current absorbed by the sample (12). Those electrons that lose energy as they pass through the sample can be used to record electron energy-loss spectroscopy (EELS) spectra as a function of probe position, which can provide information on the local electronic structure with atomic resolution (13, 14).

One of the main advantages of the TEM over the STEM is that the entire image is recorded simultaneously, with most of the electrons incident on the area of interest being used to form the image. The major disadvantage in TEM is that the image obtained does not necessarily relate to the structure in a simple manner. Image contrast is a complicated function of focus and speciment thickness, even in an aberration-corrected TEM, which means that there is no unique image that gives the best view of the structure.This makes it particularly difficult to investigate samples or defects with unknown structure or composition, which are of course the most interesting!

In contrast, probably the principle advantage of the STEM configuration, in addition to the variety of signals available, is that it is possible to obtain a *Z*-contrast image that relates far more simply to the sample structure. The *Z*-contrast image is formed by collecting the electrons scattered out to high angles on a high-angle annular dark field (HAADF) detector. The benefit is that this image is, to a very good approximation, a convolution of the intensity of the probe with an object function representing the sample in a simple manner. The underlying physical principle is that high *Z* atoms scatter to higher angles more strongly than lighter atoms. In the limit of Rutherford scattering, this goes as Z^2, so the contrast in the image will also vary approximately as Z^2. The exact contrast details will depend on the experimental set up and are affected by factors such as electron channeling or detector size. But over a fairly large ranges of defocus or sample thicknesses, the image will nonetheless represent the sample structure in a straightforward way. Thus one can obtain a qualitative understanding of all of the images presented in

1 Apr 2005 20:51 AR AR246-MR35-17.tex XMLPublishSM(2004/02/24) P1: KUV
AR REVIEWS IN ADVANCE10.1146/annurev.matsci.35.102103.090513

Annu. Rev. Mater. Res. 0.0:${article.fPage}-${article.lPage}. Downloaded from arjournals.annualreviews.org
by Oak Ridge National Lab on 06/06/05. For personal use only.

this review by considering them to be convolutions between the atomic resolution probe and a series of points at the atomic locations with a brightness of Z^2.

All of the work reported here was obtained using the two VG Microscopes' STEMs at Oak Ridge National Laboratory (ORNL), both equipped with Nion aberration correctors (14a). One of the key features of these instruments is the use of a cold field emitter as a gun. This has a number of advantages over a conventional Schottky emitter: It has a lower energy spread and a higher brightness, although the Schottky emitter has higher total current and better long-term current stability. The ORNL HB603U STEM, operated at 300 kV, produces a beam with a diameter of 0.6 Å, whereas the VG Microscopes HB501UX dedicated STEM operated at 100 kV STEM produces a beam with a diameter of 0.9 Å. The latest instrument also features a quadrupole coupling module from Nion Co. This allows the recording of energy loss spectra while collecting almost all of the electrons transmitted through the sample with better than 0.3 eV resolution, which is limited by the energy spread from the tip (15–17).

If the probe is positioned on a specific site of the specimen without scanning, a Ronchigram is formed (17a). The Ronchigram is used during the microscope alignment process. A Ronchigram is formed by collecting the transmitted electrons as a function of angle on a charge-coupled device (CCD) and can be thought of as a shadow image of the (partly transparent) sample. For an amorphous sample, this resembles a distorted BF image of the sample and directly reflects the symmetry of the microscope aberrations. For a crystalline sample, a convergent beam electron diffraction (CBED) pattern is formed, which is used to adjust the specimen orientation.

Aberrations in Electron Microscopy

Spherical aberration takes its name from light optics, where it was a common fault of the slightly too spherical shape of early lenses. It is a geometrical aberration meaning that electrons traveling at different angles to the axis are focused at different distances behind the lens. A perfect point would be focused to a disc in the image, as shown in Figure 2 (see color insert). Chromatic aberration is generated if electrons with different energies (different wavelengths) are present. Then they are focused differently depending on their energy. As any electron source will emit electrons with a range of energies, and (some electrons lose energy as they interact with the sample, this can degrade the resolution.

The aberration function is defined as the phase change across the back focal plane of the objective lens. Another equivalent and sometimes useful definition from geometric optics is that the gradient of the aberration function gives the ray displacement at the sample plane. The aberration function is normally given in a power series with angle to axis. Off axial aberrations can normally be ignored in a STEM, although we note that they have to be considered in detail when designing aberration correctors or aiming for the highest resolution with a large field of view. After aberration correction, higher-order aberrations may be significant, by which

we mean the next terms in the expansion of the aberration function; these could previously be neglected when the aberration function was dominated by spherical aberration, C_s. Therefore in a C_s-corrected system, C_5, which is the next higher order aberration becomes the dominant aberration (18). Non-rotationally symmetric aberrations also exist, of which the most common example is astigmatism.

Aberration Correction

In a modern TEM, the resolution is ultimately limited by either the spherical or chromatic aberrations of the electron lenses. Scherzer showed in 1936 (19, 20) that spherical and chromatic aberration were unavoidable for conventional rotationally symmetric magnetic lenses. These aberrations set a limit on the attainable resolution in a microscope for over 60 years. However, Scherzer assumed several conditions, namely that the optical system is round, produces a real image, does not vary with time, and has no charge on the optic axis. In 1947, Scherzer therefore proposed to overcome this limitation by breaking one of these conditions (20). Both of the aberration correctors that have recently demonstrated a practical resolution improvement rely on breaking the rotational symmetry of the system (21–26).

There are two main classes of aberration correctors, named after the type of multipole that they employ: quadrupole-octupole correctors and hexapole correctors. These multipoles, like the alignment coils in the TEM, are normally magnetic; although a chromatic aberration corrector would have to have both magnetic and electrostatic poles. Multipoles are named by their rotational symmetry (dipoles, quadrupoles, hexapoles, octupoles, etc.).

Quadrupole-octupole (QO) correctors work because octupoles have a field that varies with distance off the optic axis in the same way as does spherical aberration but has a fourfold rotational symmetry about this axis (with alternating sign on rotation by 45°). Thus the QO corrector relies on using a series of quadrupoles to distort the beam in such a way that it acquires the negative spherical aberration from the octupoles and leaves the corrector as a round beam. Three octupoles are used in order to correct the round aberration in the X, Y, and 45° directions.

Hexapole correctors, stemming from an idea by Beck (27), rely on the fact that an extended hexapole imparts spherical aberration to a round beam in addition to the primary effect of threefold astigmatism. Further refinements (28, 29) allow the projection of one hexapole to another and then into the objective lens in such a manner as to eliminate the spherical aberration without increasing off axial or higher-order aberrations.

Aberration correction, like any new field, is evolving extremely rapidly. At the time of writing, aberration correctors offer only third-order aberration correction and in general are expected to make higher-order aberrations slightly worse. The next generations of aberration correctors are already being produced and are expected to offer correction of the higher-order aberrations in order to provide better resolution and larger field of view (22).

Annu. Rev. Mater. Res. 0.0:${article.fPage}-${article.lPage}. Downloaded from arjournals.annualreviews.org
by Oak Ridge National Lab on 06/06/05. For personal use only.

1 Apr 2005 20:51 AR AR246-MR35-17.tex XMLPublishSM(2004/02/24) P1: KUV
AR REVIEWS IN ADVANCE10.1146/annurev.matsci.35.102103.090513

Annu. Rev. Mater. Res. 0.0:${article.fPage}-${article.lPage}. Downloaded from arjournals.annualreviews.org
by Oak Ridge National Lab on 06/06/05. For personal use only.

Spherical aberration correction, although initially devised for conventional TEM, may have more benefits in STEM because of the reduced sensitivity of a STEM in the *Z*-contrast mode to chromatic aberration (9, 30–32). However, just as in a CTEM, chromatic aberration correction may offer some advantages, better resolution, larger pole piece gap or more flexible designs. Kel'man & Yavor (1961) (33) showed that crossed electrostatic and magnetic quadrupole fields can produce negative chromatic aberration. Early attempts to correct the chromatic aberration of an electron microscope encountered difficulty because of the increase in spherical aberration (34), so it is likely that a combined C_s-C_c corrector would provide further benefit. The use of a monochromator would reduce chromatic abberration effects and also help improve energy resolution in EELS. The price paid for such a solution is reduced current, which then limits resolution due to an insufficient signal-to-noise ratio.

We make a distinction between aberration correction and removal of aberrations by postprocessing in the computer. Correcting aberrations through the use of hardware to alter the beam is significantly different from using postprocessing techniques to remove the effects from the image. These techniques should be regarded as quite distinct but possibly complementary.

The Corrected Electron Probe

Aberration correction has a dramatic effect on both the distribution and the spatial localization of the intensity of the electron probe. As an example, Figure 3 shows the calculated probe intensities before and after correction, with parameters based on the ORNL HB603U (these can vary depending on the microscope settings). The two probes have been normalized to the same total current and are shown on the same scale. Significant current is lost in the tails of the uncorrected probe, but

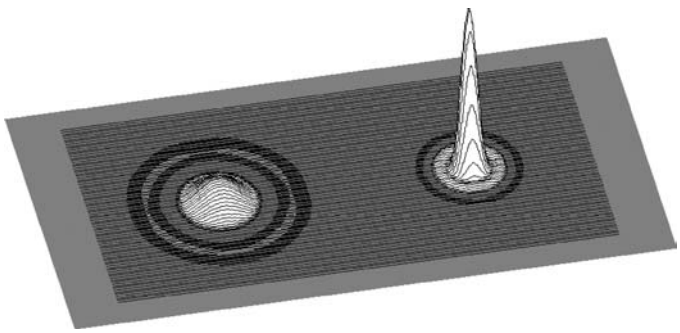

Figure 3 Calculated probe intensities before and after correction, with parameters based on the ORNL HB603U with beam energy 300 kV and energy spread 0.3 eV, (*a*) Before correction, defocus $C_1 = -63$ nm, $C_s = 1.5$ mm, $C_c = 1.3$ mm, resulting in a probe FWHM = 0.12 nm. (*b*) After correction, now $C_1 = 2$ nm, $C_s = -0.04$ mm, $C_c = 1.6$ mm and $C_5 = 100$ mm giving aprobe FWHM = 0.05 nm.

after correction the probe has a smaller full width at half maximum (FWHM), and also a far higher current density at the center. This enables not only a better spatial resolution but also the higher peak intensity gives far better sensitivity to single atoms.

Sub-Å Imaging of Crystal Lattices

The highest resolution so far accomplished with aberration-corrected STEM was by Nellist et al. (1). They demonstrated direct sub-Å resolution with the aberration-corrected HB603U at ORNL. The improved resolution allows the imaging of a Si crystal observed in the [112] direction, containing pairs of Si columns that are 78 pm apart. The imageof Si shown in Figure 4 (see color insert) was recorded in the annular dark field (HAADF) mode, and the pairs of atomic columns are seen directly resolved. The Fourier transform of this image shows clear lattice information down to 0.71 Å, and there is also apparent lattice information at 0.61 Å (1), although this is very close to the noise level of the data. This represents the highest resolution direct image ever obtained at the date of this writing.

CHARACTERIZATION OF MATERIALS IN THE ABERRATION CORRECTED STEM

In the following we review some recent examples where aberration-corrected STEM was used to investigate atomistic and electronic structures of grain boundaries, catalyst particles, single impurity atoms, and heterophase interfaces for correlation to the macroscopic materials properties.

Heterogeneous Catalysts

Heterogeneous catalysts, generally comprising of metal nanoparticles on oxide supports, are used in a large number of processes from synthesis of pharmaceuticals to automotive emission control. *Z*-contrast STEM is uniquely suited for observations of heavier species on light substrates, and with the sub-Å resolution and single-atom sensitivity achieved via aberration correction, it can provide unprecedented information about the structure of such catalysts. Most excitingly, atomic-level information obtained by STEM can then be correlated with the results of first-principles calculations and chemical reactivity measurements, thus resulting in new insights into catalytic functionality, fueling the design of more advanced catalysts for the future. This section of the review provides several examples of such studies.

CASE 1: La DOPING OF γ-Al_2O_3 γ-alumina is one of metastable polytypes of Al_2O_3 that is used extensively as a catalytic support material because of its high porosity and large surface area (35). At temperatures in the range 1000–1200°C, however,

Annu. Rev. Mater. Res. 0.0:${article.fPage}-${article.lPage}. Downloaded from arjournals.annualreviews.org
by Oak Ridge National Lab on 06/06/05. For personal use only.

1 Apr 2005 20:51 AR AR246-MR35-17.tex XMLPublishSM(2004/02/24) P1: KUV
AR REVIEWS IN ADVANCE10.1146/annurev.matsci.35.102103.090513

Annu. Rev. Mater. Res. 0.0:${article.fPage}-${article.lPage}. Downloaded from arjournals.annualreviews.org
by Oak Ridge National Lab on 06/06/05. For personal use only.

γ-alumina transforms rapidly into the thermodynamically stable α-alumina phase (corundum), drastically reducing the surface area and thus suppressing the catalytic activity of the system (36). The phase transformation can be shifted to higher temperatures by doping γ-alumina with elements such as La (37), but it was not previously possible to establish if dopants enter the bulk, adsorb on surfaces as single atoms or clusters, or form surface compounds (38–43). The lack of this information, as well as the lack of understanding of the stabilization mechanism itself, hinders performance and cost optimization of the catalytic supports. Wang and coworkers (6) used a combination of *Z*-contrast STEM and first-principle calculations to address this problem.

Figure 5*a* (see color insert) shows a *Z*-contrast image of a flake of La-doped γ-Al_2O_3 in the [100] orientation. The square arrangement of Al-O columns is clearly resolved. Single La atoms are visible in the form of brighter spots on the background of thicker but considerably lighter γ-Al_2O_3 support. Most of the La atoms are located directly over Al-O columns (site A, Figure 5*a*), but a small fraction also occupies a position shifted from the Al-O column (site B, Figure 5*a*). Note that, in this second configuration, the La atom appears much dimmer because its intensity is no longer superimposed on that of the Al-O column. Intensity variations among different La atoms on the A sites correspond to La atoms located on the entrance or the exit surfaces of the alumina flake, with the latter appearing brighter owing to electron channeling. The images reveal clearly that there is no correlation in the distribution of dopant atoms. Additional experiments utilizing a novel technique of depth slicing via focal series in STEM (see details in previous section) section g have demonstrated that La atoms are located on the surface of the alumina flakes, not in the bulk.

Density functional theory calculations have demonstrated that La atoms are strongly bound to the γ-Al_2O_3 surfaces (binding energy 7–8 eV), considerably stronger than to the α-alumina surface (binding energy 4.3 eV). In particular, the position over Al-O columns on the [100] surface of the γ-Al_2O_3 (Site A on Figure 5*a*) was identified as the lowest-energy position for the dopant, with La replacing surface Al and forcing it into a subsurface tetrahedral void (Figure 5*b*). Additionally, surface positions for La atoms are energetically preferred by as much as 3 to 5 eV per atom compared with bulk or subsurface locations. No tendency to form correlated arrays or clusters on the surface was found. Thus by comparing *Z*-contrast images and density functional theory calculations it became apparent that the stabilization is achieved by single La atoms adsorbed on the γ-Al_2O_3 surface. Dopants improve the stability with respect to the phase transition and make sintering highly unfavorable, as it would result in placing the surface La into the bulk (6).

CASE 2: Pt TRIMERS ON γ-Al_2O_3 The tendency of Pt to form trimer-like structures on the surface of γ-Al_2O_3 was observed by uncorrected STEM (44), but the precision of the experimental data on the interatomic distances was insufficient to choose among the competing mechanisms of the trimer formation. In a report by

Sohlberg et al. (45) aberration-corrected STEM was used to characterize Pt trimers in more detail. The images demonstrated that the Pt-Pt distances in the trimer differ significantly from those in bulk Pt (Figure 6*a*, see color insert), thus putting both substitutional and adatom models under doubt. A thorough theoretical study has shown that the experimentally observed geometry can be achieved only in an adatom cluster capped by an OH-group (Figure 6*b*). Additionally, it was demonstrated that unlike the metastable Pt_3 cluster, the Pt_3OH formation was stable and had a slightly electron-deficient character (Pt_3 was found to be slightly electron-rich). This finding relates directly to the Lewis acidity and catalytic activity of the Pt/γ-Al_2O_3 catalysts.

CASE 3: Au NANOPARTICLES ON TiO_2 It is remarkable that although Au is not a good catalyst in bulk or in the form of large particles, when prepared as nanoparticles on an oxide support, it becomes one of the most active catalysts for the oxidation of CO to CO_2 (46, 47). The cause of this activity has been a mystery for many years, with several explanations proposed. Early work showed that there is a correlation between particle size and activity (46), although one problem is that it is difficult to see the smallest nanoparticles by conventional TEM, hindering the identification of likely sites and mechanisms. More recent work on model systems has shown that the thickness may be more important than the lateral extent, with bilayer structures having the highest activity. Some of the models for the activity (48) required the presence of oxidized Au, but XANES revealed that in the most active catalysts, almost no oxidized Au is present.

Lupini et al. (49) used aberration-corrected STEM to show that for a highly active catalyst, most of the nanoparticles are 1–2 nm diameter, as shown in Figure 7*a* (see color insert). Quantifying the thicknesses by comparing to image simulations, including Au particle models on a substrate, revealed that these are indeed one or two layers thick. On the basis of the form of nanoparticles seen in the *Z*-contrast images, it was then possible for the first time to perform first-principles calculations to investigate the properties of realistic Au nanoparticles supported on TiO_2. These calculations revealed that the nanoparticles are anchored to oxygen vacancies on the surface, as depicted in Figure 7*b*, which allows the formation of a high areal density of nanoparticles and shows that such nanoparticles have the ability to bind both CO and O_2, unlike gold steps or surfaces. Thus it seems that the ability to bind both of the reactants is the key to the high activity of this unusual catalyst.

Application to Ceramic Materials: Si_3N_4

Silicon nitride ceramics are expected to be used in a wide variety of applications because of their superior high-temperature properties (50). The mechanical properties of Si_3N_4 are strongly influenced by the microstructure, and the introduction of high-aspect-ratio grains is well known to significantly improve fracture toughness (51). Such microstructures provide toughening mechanisms; for instance, crack bridging

Annu. Rev. Mater. Res. 0.0:${article.fPage}-${article.lPage}. Downloaded from arjournals.annualreviews.org
by Oak Ridge National Lab on 06/06/05. For personal use only.

1 Apr 2005 20:51 AR AR246-MR35-17.tex XMLPublishSM(2004/02/24) P1: KUV
AR REVIEWS IN ADVANCE10.1146/annurev.matsci.35.102103.090513

Annu. Rev. Mater. Res. 0.0:${article.fPage}-${article.lPage}. Downloaded from arjournals.annualreviews.org
by Oak Ridge National Lab on 06/06/05. For personal use only.

and pull-out and crack deflection (52). It is well understood that grain growth is controlled by the type of cations used as additives for the liquid-phase sintering process (50, 53). By this process, amorphous oxynitride intergranular films (IGF) with nanometer-scale thickness are formed. One important aspect controlling the anisotropic grain growth is the possible segregation of rare-earth dopant atoms to the amorphous/crystalline interface at the grain boundaries. Although some studies have been conducted on the growth process influenced by dopant atoms, it was only recently possible to address this point with an atomic level description (54). Shibata and coworkers used aberration-corrected STEM to image segregation of La atoms to the Si_3N_4 surfaces adjacent to the IGF.

Figure 8 (see color insert) show simultaneously recorded HAADF-STEM and bright-field STEM images of a region centered on an intergranular film. The grain on the right side of each image appears in the [0001] zone-axis orientation. The sample was tilted in an edge-on position so that the interface plane was parallel to the microscope's optic axis. Owing to the atomic number contrast in HAADF imaging, the intergranular film consisting of Si, O, N, and La atoms forms the bright vertical band in Figure 8*a*,*b*. The IGF thickness is about 1 nm, which is significantly smaller than observed in earlier studies (55, 56). Figure 8*c* shows an intensity line profile taken from the area shown in Figure 8*a*. Very high intensities in the HAADF image are observed at the IGF/Si_3N_4 interfaces, whereas somewhat lower intensities occur in the center of the amorphous film. The observed intensity line profile exhibits a bimodal distribution of La atoms at the grain surfaces, i.e., segregation. The strong image intensity along the right edge of the IGF is located where the Si column would have existed in the adjacent grain, suggesting that this zone represents the first cation layer attached to a nitrogen-terminated prismatic surface of β-Si_3N_4.

Figure 9 (see color insert) shows a magnified HAADF-STEM image of the IGF/Si_3N_4 interface. A projection view of the β-Si_3N_4 lattice model is superimposed on the image. La atoms are observed as bright intensities present at the interface and are labeled by red arrows. Figure 9*a* reveals that the positions of La atoms are shifted away from the expected positions of Si atoms based on the extension of the β-Si_3N_4 lattice, which are marked by open green circles. Bright spots within the interfacial zone, which represent La atoms, occur at distances from the nearby N atoms of the grain surface greater than the expected Si positions, indicating that La has a larger stable bond length than Si. However, some bright intensity is observable at the expected Si sites along the interface, although they are less pronounced than Si column intensities in the bulk. This suggests that at these positions nonperfect Si columns are present, which are either distorted by the amorphous film or only partially occupied by Si along the projected direction. Hence, it is concluded that the strong image intensity zone at the edge of the IGF is formed by both La and Si atoms (54).

First-principles atomic cluster calculations (54, 57) revealed three independent stable La sites per surface unit cell along the N-terminated prismatic planes of Si_3N_4. Binding energies are 0.5 to 5.3 eV higher than those for Si at its most stable

surface site. Furthermore, La—N bonds are found to be longer than comparable Si—N bonds by 0.034 to 0.048 nm. The Pixon (58) reconstructed image shown in Figure 9*b* shows strong intensity cation sites at the IGF/Si_3N_4 interface. These sites are in remarkable agreement with the theoretically predicted La sites marked with open circles.

Shibata et al. conclude that the observed enhanced anisotropic grain growth by La_2O_3 additions to liquid phase–sintered Si_3N_4 ceramics (54) derives from preferential segregation of the rare-earth atoms. The authors argue that the segregation of La to the IGF/Si_3N_4 interface and its strong bonding there hinders any further Si attachment necessary for the growth reaction, i.e., a recrystallization of Si_3N_4 out of the liquid phase. Differential binding energies and bond lengths are found to be in excellent agreement with theoretical predictions (54, 59).

Complex Alloys: Quasicrystals

Quasicrystals are intermetallic, stable compounds that exhibit a specific long-range order together with an orientational order associated with symmetry properties that are forbidden in periodic crystals. These symmetries are often described with reference to a higher-dimensional analogue of a periodic lattice. The STEM has significantly contributed to our understanding of these systems, and even though the results discussed in this section are previous to the aberration correction era, they still show a good example of how the STEM can provide unique information (60).

By performing angle-resolved and/or in situ heating/cooling experiments, ADF-STEM now can determine not only the atomic structure but also the local thermal vibration amplitudes in a solid that crucially affect the physical properties of materials. Direct, real-space imaging of a local thermal vibration anomaly in a solid has been demonstrated for the first time, through atomic-resolution ADF-STEM observations of an $Al_{72}Ni_{20}Co_8$ quasicrystal (61). This is a decagonal quasicrystal, periodic in one direction and quasiperiodic in the perpendicular plane. Significant changes of ADF contrast were seen at specific Al sites depending on the observation temperature as well as the angular range of the detector (see Figure 10). At 110 K a local anomaly of atomic vibrations becomes significant at specific atomic sites in the structure (Figure 10*b*). The distribution of these localized vibrations is not random, but quasiperiodically correlated, with a length scale of 2 nm. The origin of this anomalous contrast is well-explained by changes in the Debye-Waller factor. This implies a change in the mean-square thermal vibration amplitude of the atoms at these specific sites, a local thermal vibration anomaly. The long-range distribution of these specific Al sites can be interpreted in terms of quasiperiodically equivalent atomic sites defined within the framework of hyperspace crystallography. These observations are directly relevant to a key issue concerning lattice dynamics in a quasicrystalline solid: the nature of the phason—the phason is an extra elastic degree of freedom specific to the quasicrystals (in addition to the usual phonons in crystals) and has been theoretically predicted to cause localized fluctuations.

Annu. Rev. Mater. Res. 0.0:${article.fPage}-${article.lPage}. Downloaded from arjournals.annualreviews.org
by Oak Ridge National Lab on 06/06/05. For personal use only.

1 Apr 2005 20:51 AR AR246-MR35-17.tex XMLPublishSM(2004/02/24) P1: KUV
AR REVIEWS IN ADVANCE10.1146/annurev.matsci.35.102103.090513

Annu. Rev. Mater. Res. 0.0:${article.fPage}-${article.lPage}. Downloaded from arjournals.annualreviews.org
by Oak Ridge National Lab on 06/06/05. For personal use only.

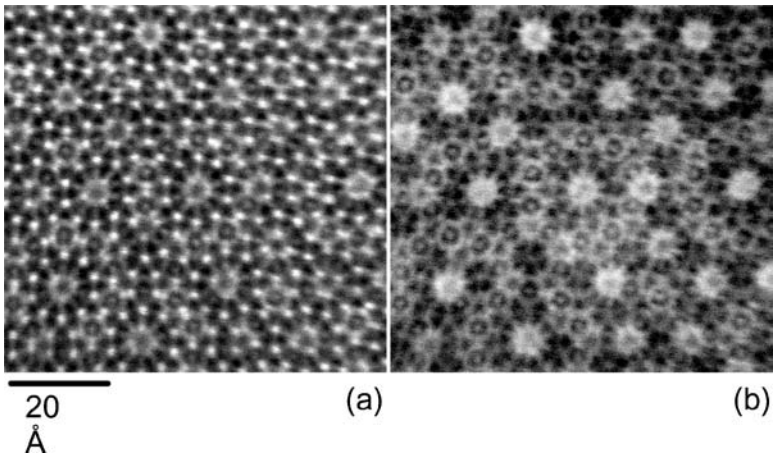

Figure 10 *Z*-contrast images of an $Al_{72}Ni_{20}Co_8$ quasicrystal viewed along the decagonal axis. (*a*) High-angle range (inner-angle ∼50 mrad) showing transition metal columns bright, Al columns less bright. (*b*) Low-angle range (inner-angle ∼35mrad), showing Debye-Waller factor contrast quasiperiodically correlated (61).

Embrittlement of Structural Alloys: Bi in Cu

Embrittlement of copper by bismuth is the classic example of the phenomenon and a nearly ideal system for an atomic-scale investigation of embrittlement. Only two elements are involved, no Cu-Bi intermetallic compounds exist, and there is no evidence that hydrogen embrittles copper. Figure 11 (see color insert) (62) compares *Z*-contrast images of the nondoped (*a*) and the Bi-doped (*b*) boundaries. In this [001] projection, the atomic columns in the copper grains form a square grid of bright dots separated by 0.18 nm. The boundary in both samples is seen to consist of a periodic array of a defect structural unit (as indicated in Figure 11). One of the four undercoordinated atomic columns in each structural unit of the bismuth-doped boundary is seen to be distinctly bright. The extra intensity is consistent with the presence of an impurity with an atomic number much greater than copper, in this case Bi. The images make it clear that this grain boundary configuration is little affected by the presence of bismuth. No new phases are formed, and no drastic atomic rearrangements occur as the result of bismuth segregation to this boundary. Bismuth simply substitutes for Cu on a preferred atomic site in the boundary core. The electronic structure of the grain boundary region can be measured directly with EELS. It is found that locally the Cu-L_3 edge is affected by the presence of bismuth in the boundary. Three small peaks superimposed on the step-like Cu-L_3 edge are found to be considerably reduced in the spectrum from the doped boundary (62). This observation indicates a change in bonding of the copper atoms at the doped grain boundary. These changes are consistent with a reduction of the density of *d*-like states at the Fermi level and reduced hybridization between *d* and *s* states

Annu. Rev. Mater. Res. 0.0:${article.fPage}-${article.lPage}. Downloaded from arjournals.annualreviews.org
by Oak Ridge National Lab on 06/06/05. For personal use only.

for the copper atoms that surround the bismuth. Both of these results also imply reduced covalent (directional) bonding between Cu 3*d* electrons in the boundary region.

The choice of a small period tilt boundary makes it possible to combine high-resolution imaging and spectroscopy with first-principles calculations. Density functional calculations of the Cu L_3 edge in the Bi-doped grain boundary show a reduction of all three maxima in near-edge structure, compared with the calculated near-edge structure for bulk Cu, just as was seen experimentally. The calculations confirmed the interpretation of the experimental EELS results, i.e., there are a reduced number of unoccupied *d* holes at or above the Fermi level and reduced hybridization between *d* and *s* states for the copper atoms that surround the bismuth impurities. The calculated charge density difference also revealed that bismuth induces a slight reduction in the directionality of bonding between Cu atoms. In addition, the calculations show enhanced electron density at the copper sites that surround the Bi impurity (62). This means that electrons further fill the usually half-filled *s*-bands of copper. This *s*-band filling can be described as a population of antibonding states, which reduces the bond strength between the copper atoms that surround the bismuth impurity.

Using a combination of *Z*-contrast imaging, EELS, and ab-initio theoretical materials simulations, the geometric and electronic structure of a grain boundary with and without the impurity can be investigated on the atomic scale. By knowing the atomic configuration, reliable electronic structure calculations can be made to determine how the impurity affects bonding and induces embrittlement. This investigation revealed that copper atoms surrounding the segregated bismuth exhibit a closed 3*d* shell, reduced *s*-*d* hybridization and an *s*-band that is more than half full.

The improved resolution that aberration correction offers will expand the number of boundaries that can be imaged. Atomic column positions will be revealed with more contrast and better signal-to-noise ratio with correction, thus increasing the detectability of segregants. However, the most exciting development is the possibility of imaging the atomic configurations of defects in all three dimensions that will come with further improvements in aberration correction. This development will make it possible for electron microscopy to move beyond the limits set by the projection problem and allow the determination of the atomic positions and compositions in X, Y, and Z directions of any boundary or defect.

Complex Oxide Characterization in the STEM

Many different complex oxides are of wide interest to electronics and the emerging field of spintronics. Most, such as ferroelectrics, high T_c superconductors, or colossal magnetoresistant materials, have a perovskite structure. In these materials, the aberration-corrected STEM has successfully achieved the imaging of light atoms, such as O. Seeing oxygen columns is quite a significant achievement in microscopy, which is also of enormous relevance in complex oxide science. Oxygen columns can be now resolved in the HAADF images in the STEM, even when they are surrounded by heavier columns. As an example, Figure 12 (see color

1 Apr 2005 20:51 AR AR246-MR35-17.tex XMLPublishSM(2004/02/24) P1: KUV
AR REVIEWS IN ADVANCE10.1146/annurev.matsci.35.102103.090513

Annu. Rev. Mater. Res. 0.0:${article.fPage}-${article.lPage}. Downloaded from arjournals.annualreviews.org
by Oak Ridge National Lab on 06/06/05. For personal use only.

insert) shows an image from $SrTiO_3$ in the [110] orientation where the light oxygen atomic columns can easily be seen.

Perovskite materials in general are highly suitable candidates for EELS analysis, due to the wide availability of theoretical reports and computational techniques needed for the interpretation of the local density of states and, therefore, of the EEL spectra. Also, one of the great advantages of aberration correction in the STEM is the higher intensity and spatial localization of the electron probe. As shown earlier, not only is the probe more spatially localized, but also the intensity is higher. This is a key issue when it comes to carrying out atomic resolution EELS: the signal increases, which allows shorter acquisition times and reduction of beam damage, and the excited volume decreases, which allowis a true column-by-column probe of the material's electronic properties (2, 3, 63).

Figure 13*a*, see color insert, shows a high resolution *Z*-contrast image of a La single atom from a one-unit-cell thick $La_{0.002}Ca_{0.998}TiO_3$ layer in a $CaTiO_3$ matrix (4). The higher *Z* of La as opposed to Ca, O, or Ti, makes single La atoms appear as bright spots in this environment, although this brightness is dependent on atom depth, as discussed below (32, 64). By placing the STEM probe directly over the image of an isolated La atom, a clear EELS signature is obtained. In Figure 13*b*, the red spectrum shows two distinct peaks that correspond to the La $M_{4,5}$ lines at 832 and 849 eV. The intensity is low, as one would expect from the small number of counts associated with the excitations of a single atom, but clearly observable.

There has been much discussion in recent years about detection limits and the role that the delocalization of the underlying ionization process plays in limiting the resolution of the STEM (3, 14, 65–67). In order to analyze the localization of the EELS signal, Varela et al. performed line scans across the individual La cations (4). Figure 13*a* shows the directions of the scan with respect to the atom position. Given the fact that neighboring atomic columns correspond to different atomic species (O or TiO columns), the channeling and therefore the localization of the signal would be different. As depicted in Figure 13*b*, the EELS signal attributed to the La single atom is clearly localized on the atomic column containing this ion. When the electron beam is placed on any adjacent column, the signal is substantially reduced, to only $(10 \pm 5)\%$ on the neighboring TiO column, and to $(20 \pm 5)\%$ on the neighboring O site, only 0.19 nm away (shown in blue). This clearly indicates that the La can be localized to significantly better than 0.2 nm. The impact parameter for La-M excitation is $\sim$0.01 nm (3), which suggests that the residual intensity from neighboring columns is almost certainly the effect of dechanneling (68, 69).

Through dynamical simulations of probe spreading, an indication of atom depth was also obtained. EELS images were simulated using mixed dynamic form factor theory (68, 69). To estimate the depth of the impurity, Figure 13*c* shows the simulated signal strength for an aberration-free probe situated on the Ca column, O column, and TiO column as a function of the impurity depth. (A simplified cubic model for the structure was used for this simulation). The contribution on the Ca column initially increases through to the electrostatic attraction of the electron to the column (channeling), but then decreases as elastic and inelastic scattering

Annu. Rev. Mater. Res. 0.0:${article.fPage}-${article.lPage}. Downloaded from arjournals.annualreviews.org
by Oak Ridge National Lab on 06/06/05. For personal use only.

mechanisms broaden the probe. As a function of dopant depth in the crystal, the contribution of the dopant atom to the EELS intensity on the O column rises gradually; simulations of the electron density make clear that this is due to probe spreading. From this figure it is estimated that a (20 ± 5)% signal on the O column results from an impurity depth of around 10 nm. From EELS simulations, show in Figure 13*c*, the impurity depth was estimated to be 12.2 nm. The simulations support the localization of the ionization interaction and demonstrate that the dynamical propagation, in transferring some electron intensity to adjacent columns, is responsible for the signals obtained. This level of sensitivity allows us to analyze in great detail the structure and electronic structures of complex oxides at the atomic scale.

CASE 1: CHARGE ORDERING IN MANGANITES A representative example concerns the study of charge ordering in manganese oxides exhibiting colossal magnetoresistance (CMR) (70). In some of these manganites a form of spatial modulation known as the charge-ordered state is encountered. These phases are insulating and are often antiferromagnetic so that understanding the origin of the phenomenon may provide the key to the origin of ferromagnetism and CMR in these materials. However, in spite of extensive studies dedicated to this topic, the underlying physics remains an open issue (70–74). So far, experimental techniques, such as diffraction and scanning probe microscopy, have provided only limited information, averaged over long-length scales and confined to the materials surfaces, respectively. CMR materials have a chemical formula of $A_xB_{1-x}MnO_3$, where A is a trivalent cation (La, Nd, Bi, Pr) and B a divalent cation (Sr, Ca, Ba). A HAADF image of a $Bi_{0.37}Ca_{0.63}MnO_3$ (BCMO) manganite is shown in Figure 14*a* (see color insert) along the (100) direction (75). MnO planes have been marked with blue dotted lines; BiCa planes are marked with yellow lines. The columns with a higher Bi concentration are brighter, whereas the Ca-rich columns are darker. No chemical ordering was observed from these images. But, interestingly, the resulting mixed-valence state within the Mn sublattice produces a complex electronic structure that we can image using EELS. The common view so far is that a fraction 1-x Mn ions per unit cell are in a +4 formal oxidation state, with a $3d^3$ electronic configuration ($t_{2g}{}^3\ e_g{}^0$), whereas the rest, being Mn^{+3}, have a $3d^4$ configuration $(t_{2g}{}^3 e_g{}^1)^1$. The charge-ordered state is believed to arise as a spatial stabilization of the e_g orbital distribution. For the BCMO compound the transition temperature to a disordered state is above room temperature making it unnecessary to cool the sample to observe charge ordering.

EELS can probe the occupancy of the outer *d*-states of the Mn atoms with atomic resolution. The white lines at the onsets of the L_3 and L_2 [absorption edges of transition metals are a characteristic signature of electronic transitions from the $2p_{1/2}$ and $2p_{3/2}$ Mn core states to unoccupied *d*-like states near the Fermi level (76–80). In particular, the ratio of the intensity of the L_3 peak to the L_2 peak, the L_{23} ratio, increases as the formal Mn oxidation number decreases. For example, Mn atoms in the parent compounds $LaMnO_3$ and $CaMnO_3$ have a +3 and +4 formal oxidation states ($3d^4$ and $3d^3$ configurations), respectively. EEL spectra

Annu. Rev. Mater. Res. 0.0:${article.fPage}-${article.lPage}. Downloaded from arjournals.annualreviews.org
by Oak Ridge National Lab on 06/06/05. For personal use only.

for those are shown in Figure 14*b*. The value of the L_{23} ratio in the first case is $L_{23} = 2.7 \pm 0.2$, whereas in the second, it is $L_{23} = 2.1 \pm 0.2$. In the experiment reported by Varela et al. (75), noticeable variations of this ratio can be observed as the electron beam is swept across the sample. Typical EEL spectra from two inequivalent types of Mn columns are shown in Figure 14*b*. The L_{23} ratios are again 2.7 ± 0.2 and 2.1 ± 0.2, just as found in the parent compounds $LaMnO_3$ and $CaMnO_3$ respectively. These data therefore establish that the Mn atoms in BCMO coexist in two distinct formal oxidation states, +3 and +4. Further confirmation of the oxidation state is seen from the chemical shifts. In both the mixed valent manganite and the parent $LaMnO_3$ compound a shift of approximately 1 eV is observed to lower energy losses.

Figure 14*c* shows the variation of the L_{23} ratio with position in the sample as the beam is swept parallel to the pseudocubic [100] direction (green arrow in Figure 14*a*). Clearly, the L_{23} ratio exhibits a modulation with a periodicity varying between 11 Å and 15 Å. When rotating the scanning direction by 90° (blue arrow in Figure 14*a*) *no* spatial modulation of the Mn L_{23} ratio was observed (Figure 14*d*), which points to a stripe-like geometry for the *3d* occupancy ordering. Additional scans were performed at different angles to confirm this conclusion. For example, the results obtained for a 45° angle revealed a modulation of the L_{23} ratio with a period of 22 Å (Figure 14*e*), close to the projection of the initially measured modulation length along a direction at 45°. This is consistent with the existence of a family of inequivalent planes or stripes that run along the pseudocubic (100) planes.

Higher magnification data along the [100] cubic axis are shown in Figure 14*f*, where individual Mn planes have been marked with red arrows. Jumps in the L_{23} ratio are visible only on specific individual Mn planes. From similar line scans (Figure 14*g*), the stripe width was measured to be below 3 Å, evidence that the stripes are atomically wide. Also, the uneven spacing between maxima in Figure 14*f* is noticeable, showing how the incommensurate number of doping electrons per unit cell cannot be accommodated in an equi-spaced striped pattern. Fourier transforms of the L_{23} ratio data showed clear peaks at frequencies around 0.83 $Å^{-1}$, denoting a spatial periodicity of about 12 Å. The stripe geometry evidenced by EELS is perfectly consistent with the macroscopically averaged periodicity observed in electron diffraction (75).

Interfaces

Most of the physical properties of composite materials are determined by low-dimensional active regions such as interfaces or grain boundaries. Hence, the understanding of the relations between their nature, electronic properties, and macroscopic behavior requires the use of probes with ultimate atomic resolution. A complete understanding of the atomistic and electronic structure of an interface can be used to predict physical properties and assist the development of new interfaces with unique properties. A few examples of atomic resolution studies of complex oxides and of the relationship between structure and electronic properties of oxide interfaces are presented below.

Annu. Rev. Mater. Res. 0.0:${article.fPage}-${article.lPage}. Downloaded from arjournals.annualreviews.org
by Oak Ridge National Lab on 06/06/05. For personal use only.

CASE 1: SUPERCONDUCTING/FERROMAGNETIC SUPERLATTICES The first example concerns the analysis of interfaces in superconducting/ferromagnetic $YBa_2Cu_3O_{7-x}/La_{0.67}Ca_{0.33}MnO_3$ (YBCO/LCMO) superlattices. Experimental studies on LCMO/YBCO structures suggest a strong interplay between ferromagnetism and superconductivity that results in the injection of spin polarized carriers (81) or other proximity phenomena, which occur at nanometer distances from the interface (82–86). The critical temperatures Tc of thin high Tc superconducting films sandwiched between CMR spacers are comparatively lower than those obtained when using a non-magnetic material. Furthermore, heterostructures with ultrathin YBCO layers (one or two unit cells thick) are non-superconducting (82, 83). A deep understanding of the physics of oxide-based superconducting/ferromagnetic heterostructures needs a careful analysis of the relation between interface structure and electronic properties at the atomic scale. Recently, a detailed analysis of the structure/property relations at such interfaces has been reported by Varela et al. (87, 88). The structural quality of the samples was shown to be rather high. The YBCO/LCMO interface is coherent and free of defects, as seen in Figure 15. Occasionally, several steps one unit cell high are observed consistent with the small

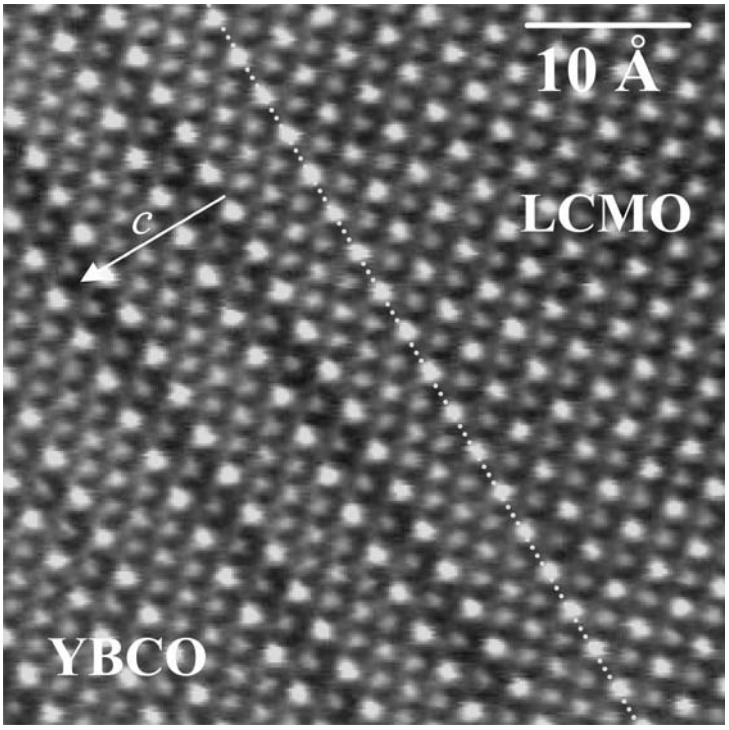

Figure 15 High-resolution *Z*-contrast image of a typical YBCO/LCMO interface. The dotted line marks the interface position.

1 Apr 2005 20:51 AR AR246-MR35-17.tex XMLPublishSM(2004/02/24) P1: KUV
AR REVIEWS IN ADVANCE10.1146/annurev.matsci.35.102103.090513

Annu. Rev. Mater. Res. 0.0:${article.fPage}-${article.lPage}. Downloaded from arjournals.annualreviews.org
by Oak Ridge National Lab on 06/06/05. For personal use only.

step disorder found by X-rays (82, 83). EELS studies conclude that there is no major chemical interdiffusion (87).

Once structural effects were ruled out as a source of T_c reduction in these samples, the study of the interface electronic properties found several interesting effects. Direct evidence for charge transfer, i.e., doping of carriers from the ferromagnet into the superconductor, has been shown. Spectroscopic measurements with atomic resolution show the existence of a noticeable decrease in the density of holes in the YBCO by the interface. In HTCS materials, the O 2*p* and the Cu 3*d* bands lie very close to the Fermi energy. Therefore, the analysis of the O K edge at 530 eV and the Cu L edge at 930 eV has proven to be very useful to illuminate their electronic properties. In particular, the oxygen K edge, which results from exciting transitions from the oxygen 1*s* core level to the oxygen 2*p* bands can be used to quantitatively probe the occupancy of the oxygen 2*p* bands, i.e., the carrier density in the superconductor (89, 90). The prepeak in Figure 2*b* contains mostly O 2*p* band contribution. The ratio of the prepeak to the main edge provides a quantitative measure of the local density of holes. Figure 16*a* shows the prepeak intensity as a function of distance to the interface, within the YBCO, in a [YBCO $_{10\ u.c.}$/LCMO $_{15\ u.c.}$]1000Å superlattice. Right on the interface plane, the hole density in the superconductor is reduced, and it then slowly increases till it achieves the bulk value at 3 nm from the interface. Also, the Mn oxidation state within the adjacent LCMO layer was found to be slightly higher (by ~5%) than the value expected for the given chemical doping. This situation is consistent with having some electron doping from the manganite into the superconductor. Very likely, this is the origin of the 3-nm-thick hole-depleted layer in the YBCO side of the interface. These results should be taken into account when trying to understand the reduced T_c values in these superlattices.

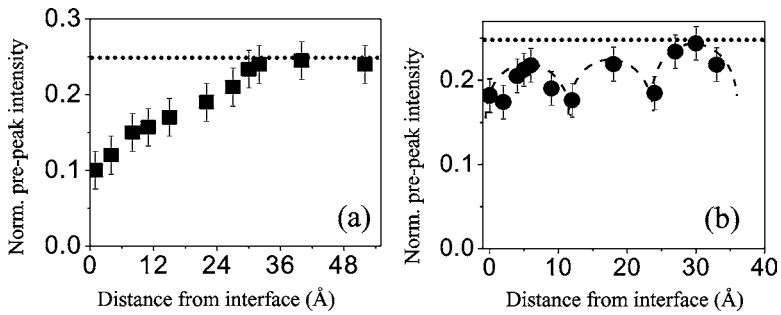

Figure 16 (*a*) Normalized prepeak intensity for the O K edge acquired at the YBCO side of a YBCO/LCMO interface, as a function of the distance to the interface. The horizontal dotted line marks the prepeak intensity in bulk YBCO. (*b*) Normalized prepeak intensity within the YBCO in a YBCO/PBCO interface, as a function to the distance to the interface.

Annu. Rev. Mater. Res. 0.0:${article.fPage}-${article.lPage}. Downloaded from arjournals.annualreviews.org
by Oak Ridge National Lab on 06/06/05. For personal use only.

The situation in a superconducting/insulator $YBa_2Cu_3O_{7-x}/PrBa_2Cu_3O_7$ (YBCO/PBCO) interface is quite different, as summarized in Figure 16*b*, where again the hole density in the superconductor versus the distance to the interface is plotted. In this case, the CuO_2 planes in the first YBCO unit cell by the interface already show a doping level close to optimal. Interestingly, EELS measurements in these samples show a spatial oscillation of the density of holes with a period equal to the lattice parameter, $c = 11.7$ Å. The hole density decreases on the CuO chains, whereas it increases on the CuO_2 planes to match the bulk value. These measurements, which were also reproduced in YBCO thick films, constitute a direct proof that the holes responsible for superconductivity are localized within the CuO_2 planes, in agreement with the commonly accepted belief.

CASE 2: ELECTROCERAMICS Another very interesting example comes from electroceramic materials, also with perovskite structure. These are gaining increasing importance for technological applications as functional ceramics in electrical and microelectronic devices (91–94). By contacting these functional ceramics with typically 3*d* transition metals, the resulting metal/ceramic interfaces are known to strongly affect the electronic and mechanical properties of such devices (95, 96). From the point of view of fundamental science, metal/perovskite interfaces represent contacts between two materials with different bonding mechanisms: a metal with a purely metallic bonding characteristic and a perovskite with mixed ionic-covalent bonds (97–99).

The $Pd/SrTiO_3$ interface was chosen as a model system in which the face-centered cubic transition metal is in contact with the (100) surface of $SrTiO_3$, which crystallizes in the cubic perovskite structure at room temperature. HAADF imaging, high-spatial resolution EELS, and density functional theory in the local density approximation (100, 101) were applied to delimit how adhesion is achieved at metal/perovskite interfaces (102).

Thin Pd films with a nominal thickness of 35 nm were deposited on (100) surfaces of single crystalline $SrTiO_3$ by molecular beam epitaxy. The (100) surface of cubic $SrTiO_3$ can either be terminated either by a TiO_2 or by a SrO layer. Ion etching of the substrate in a buffered HF solution and subsequent heating cycles prior to deposition resulted in a TiO_2-terminated surface (103, 104). TEM observations showed Pd islands on the substrate surface with an epitaxial orientation relationship with (100) planes and ⟨100⟩ directions in both materials parallel to each other. Figure 17 shows an HAADF image of the $Pd/SrTiO_3$ interface in ⟨100⟩ zone-axis orientation, recorded with the HB603U STEM (102). A coherent interface structure as well as the epitaxial cube-on-cube orientation relationship between the Pd film and the $SrTiO_3$ substrate is observed. An analysis of relative image intensities for the atomic columns indicate that the interface is terminated by a TiO_2 layer rather than by SrO (Figure 17, see color insert). No interfacial area with a SrO termination was observed throughout all the recorded data sets, although some areas with free SrO-terminated surfaces were observed. Thus the conclusion is that Pd prefers to nucleate on TiO_2-terminated (100) $SrTiO_3$ surfaces, which is in perfect agreement with theoretical predictions by Ochs et al. (105, 106), who

1 Apr 2005 20:51 AR AR246-MR35-17.tex XMLPublishSM(2004/02/24) P1: KUV
AR REVIEWS IN ADVANCE10.1146/annurev.matsci.35.102103.090513

Annu. Rev. Mater. Res. 0.0:${article.fPage}-${article.lPage}. Downloaded from arjournals.annualreviews.org
by Oak Ridge National Lab on 06/06/05. For personal use only.

found the Pd adsorption on the TiO_2-terminated substrate surface to be energetically favored compared to the nucleation on a SrO-terminated substrate surface. Ochs and coworkers also predicted an adsorption of Pd atoms on top of oxygen atoms of the (100) surface rather than above Ti atoms and the adjacent hollow sites.

To investigate this aspect in more detail, van Benthem and coworkers (102, 107) used fully relaxed atomistic structure models provided by Ochs et al. for the two different interface terminations (105) to calculate site- and symmetry-projected densities of unoccupied states (PDOS). The calculations were performed with a mixed-basis pseudopotential approach (107–109). To a good approximation the calculated O p-PDOS are proportional to electron energy-loss near-edge structures (ELNES) of O K absorption edges. van Benthem et al. (102, 110) measured the O K-, the Ti $L_{2,3}$, and the Sr $L_{2,3B}$ absorption edges in electron energy-loss spectra with a high-spatial resolution to evaluate the theoretically predicted structure models. Figure 18 (see color insert) shows the O K-edge for bulk $SrTiO_3$ with high energy resolution (*a*) in comparison with the O K-edge measured from a 2 $\times$ 20-nm area containing the interface (*b*). The interfacial O K-edge reveals four major spectral peaks labeled A, B, C, and D characteristic of the bulk (Figure 18), along with an additional spectral feature X_3. The peak labels are chosen to coincide with a more detailed spectral analysis in references (107) and (110).

The interface spectrum (Figure 18*b*) still contains some contributions from oxygen atoms in bulk $SrTiO_3$ substrate. To extract the purely interface-related signal, the contribution of bulk spectral intensity to the interface spectrum was estimated to be 11% through the quantitative spatial difference technique (111–114). This estimate is based on geometrical considerations and beam broadening effects within the transmitted specimen. The extracted interface-specific component is plotted in Figure 18*c*. Because the signal-to-noise ratio of this spectrum is rather small, it was smoothed with a 1.0 eV-wide top-hat function and then plotted in Figure 18*d*. The interface specific line shapes in Figure 18*c*,*d* clearly show a damping of the pure bulk intensities A, B, C, and D along with the appearance of new spectral features labeled X_1, X_2 and X_3, which are absent in the bulk (see Figure 18*a*).

Comparing first the calculated line shapes with the experimental ELNES data for bulk $SrTiO_3$ (i.e., spectra a and h), it can be inferred that the calculated PDOS reproduces the experimental ELNES data (102, 107). Focusing on the interface specific components of the O K-ELNES (see Figure 18*c*,*d*), a high level of agreement is observed with the calculated PDOS for the TiO_2-termination plotted in Figure 18*e*. The calculated data not only reproduces the general ELNES line shape concerning the bulk peaks A, B, and C, but also clearly exhibits the peaks labeled X_1, X_2, and X_3 as observed by experiment. The calculated PDOS obtained from the SrO-terminated structure model (Figure 18*f*) does not show any agreement with the experimental data (Figure 18*c*,*d*). Especially, in the energy regime where peak X_3 was observed, the densities of states at the SrO- terminated interface exhibits a minimum, which is contrary to the experimental findings. Therefore, it is concluded that the experimentally observed Pd/$SrTiO_3$ interface is characterized by a TiO_2 termination of the substrate surface. This is in good agreement with the direct observations by HAADF-STEM imaging (102, 110).

1 Apr 2005 20:51 AR AR246-MR35-17.tex XMLPublishSM(2004/02/24) P1: KUV
AR REVIEWS IN ADVANCE10.1146/annurev.matsci.35.102103.090513

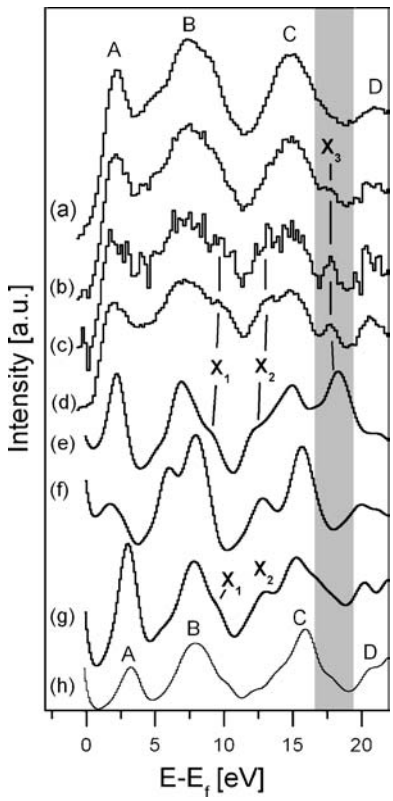

Figure 18 Experimentally and theoretically determined O K-edges recorded from bulk $SrTiO_3$ (*a*) and from a 2 × 20-nm^2 area containing the Pd/$SrTiO_3$ interface (*b*). The interface-specific component of (*b*) is plotted in (*c*) and (*d*), before and after smoothing of the curve, respectively. Line profiles (*e*) and (*f*) are the calculated O p-PDOS for a TiO_2- and a SrO-terminated interface structure. Spectrum (*g*) is the calculated O p-PDOS for the free TiO_2-terminated $SrTiO_3$ surface; (*h*) is the O p-PDOS in bulk $SrTiO_3$. All spectra are plotted as a function of energy relative to the Fermi level E_F.

Figure 19 is a sketch of the local oxygen atom coordination in bulk $SrTiO_3$ (*a*), at the $TiOB_{2B}$-terminated surface, (*b*) and at the Pd/$SrTiOB_{3B}$ interface (*c*). Because oxygen atoms are coordinated by either four Sr atoms, two Sr atoms, or two Sr atoms plus one Pd atom, the crystal fields at the oxygen sites are different for the three arrangements. A detailed analysis of the corresponding p_x, p_y and p_z projected PDOS data revealed that the crystal fields at the interfacial O sites are modified compared with those of bulk $SrTiO_3$. This results in a reduced splitting of the peaks labeled C and D in Figure 18*a*, hence forming the extra peak X_3.

The agreement of the experimental electronic structure results with the calculated unoccupied densities of states positively evaluates the validity of the theoretically predicted atomistic structure model (102). Therefore, it is germane to determine the bonding characteristics across the interface in terms of the calculated occupied densities of states. The occupied PDOS shows a strong overlap of O p_z orbitals and Pd 4d orbitals across the interface. Hence, the adhesion between the (100) $SrTiO_3$ surface and the Pd film is determined by a hybridization of O p_z and Pd 4d states, establishing σ-type bonds. Parallel to this effect, an increased overlap of the O p_xPDOS with the Ti $3d_{x^2-y^2}$ PDOS can be observed, reflecting

Annu. Rev. Mater. Res. 0.0:${article.fPage}-${article.lPage}. Downloaded from arjournals.annualreviews.org
by Oak Ridge National Lab on 06/06/05. For personal use only.

1 Apr 2005 20:51 AR AR246-MR35-17.tex XMLPublishSM(2004/02/24) P1: KUV
AR REVIEWS IN ADVANCE10.1146/annurev.matsci.35.102103.090513

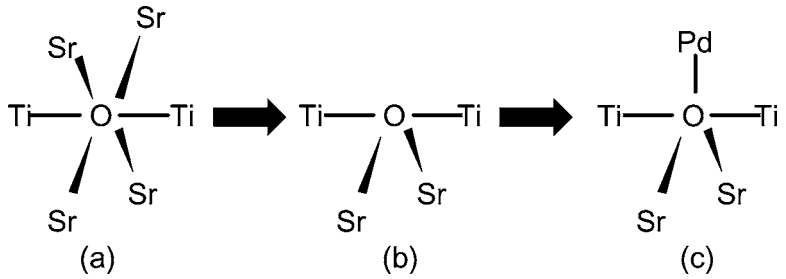

Figure 19 Sketch of (*a*) bulk, (*b*) free surface, and (*c*) interface models showing the ligands for the interfacial oxygen atoms. The modification in the coordination of interfacial oxygen columns when forming the $Pd/SrTiO_3$ interface changes the crystal field. The modified ligand field is responsible for the appearance of peak XB_{3B} in Figure 18.

an increased bonding between O and Ti within the substrate surface (102, 107). However, Ti $3d_{x^2-y^2}$ to Pd $4d_{xy/xz}$ interactions are also observable and contribute weakly to the adhesion (107).

In summary, a combination of aberration-corrected HAADF-STEM imaging, high- spatial resolution EELS, and ab initio calculations resulted in a complete determination and understanding of the origin of adhesion forces at the $Pd/SrTiO_3$ interface.

Three-Dimensional Imaging of Semiconducting Interfaces

The dimensions of silicon-based semiconductor devices have been reducing steadily over the past few decades, as frequently described by Moore's law (115–117). Owing to the shrinking dimensions, which are close to the atomic scale, the presence of single-dopant atoms in gate dielectric films and interconnects derives ever more significance (117). Even a single impurity atom at the interface between Si and a high dielectric constant (high-*k*) film can introduce defect states into the local band structure (118) and therefore significantly alter the interface properties, such as the complex dielectric function, leakage current, and breakdown field. Similarly, it can introduce scattering centers into the Si gate which can reduce the carrier mobility. Early work on imaging dopant atoms relied on statistical arguments to show that the imaged dopant atoms are in the bulk (119), and work done at lower resolution has used approximate matches to image simulations (120), neither of which is unequivocal proof for the location of the dopants. It has been largely overlooked that the tremendously decreased spot sizes, δ_s, due to aberration-correction of the probe-forming lenses, also result in a significantly reduced depth of focus T in the STEM (121).

$$T \leq \frac{\delta_s}{\alpha} = \frac{\lambda}{\alpha^2}, \qquad 1.$$

Annu. Rev. Mater. Res. 0.0:${article.fPage}-${article.lPage}. Downloaded from arjournals.annualreviews.org
by Oak Ridge National Lab on 06/06/05. For personal use only.

Annu. Rev. Mater. Res. 0.0:${article.fPage}-${article.lPage}. Downloaded from arjournals.annualreviews.org
by Oak Ridge National Lab on 06/06/05. For personal use only.

where α is the illumination semi-angle and λ is the electron wavelength. The equation shows that the availability of larger illumination angles decreases the depth of focus much faster than it improves the lateral resolution. Hence, only very thin slices of the specimen (2–3 nm thick) come into focus at a time. By recording image stacks at different focus values it is possible to "slice" through the TEM sample in a manner comparable to that used in confocal optical microscopy (15). With the HB603U STEM, a volume resolution better than 0.08 nm $\times$ 0.08 nm $\times$ 4 nm is achievable (122), i.e., approximately a factor of 10^{12} higher than in X-ray tomography (123–125) and a factor of 100 higher than recent electron tomography techniques based on tilt-series reconstruction (126–128).

Hafnium dioxide (HfO_2) is a high-k material ($k = 25$) under consideration as a replacement for SiO_2 ($k = 3.9$) as a gate dielectric. For this study, approximately 6-nm-thick HfO_2 films were deposited on Si substrates using atomic layer deposition (129) at a temperature of 320°C. The samples were then rapid-thermal annealed at 950°C for 30s in N_2 and afterward capped with undoped polycrystalline Si by chemical vapor deposition. To avoid artifacts from ion milling, samples were prepared for cross-sectional TEM purely by mechanical polishing. Both imaging and EELS measurements revealed a thin, thermally grown SiO_2 interlayer in between the polycrystalline HfO_2 film and the silicon substrate. High-resolution ADF STEM imaging revealed single Hf atoms within the SiO_2 interlayer (122). Figure 20 (see color insert) shows 9 images extracted from a 41-frame through-focal-series recorded in $\langle 110 \rangle$ zone-axis orientation. The full series was acquired in less than 5 min. At various positions throughout the series single Hf atoms appear and disappear over about 3 to 5 frames, each corresponding to intervals of 1.5 nm to 2.5 nm in depth (see for instance the red circle in Figure 20). To demonstrate the location of the Hf atom marked in Figure 20 more clearly, Figure 21 (see color insert) shows a projection view of the three-dimensional data cube.

The image in the x-y plane reveals the polycrystalline HfO_2 layer separated from the Si substrate by a roughly 1-nm-thick SiO_2 layer. The single Hf atom visible in the x-y plane is also observed in the x-z plane and the y-z plane as a single atom, visible about half way through the z -range of the acquired data set. The voxels in the data set are not cubic but cuboid due to the limited vertical resolution compared with the high lateral resolution. Throughout the whole data set, the two vertically outermost Hf atoms are about 6 $\pm$ 1 nm apart from each other (122). We assume that these two atoms sit at the top and bottom surfaces of the TEM specimen. As a result, the sample thickness can thus be estimated to be 6 $\pm$ 1 nm.

The through-focal-series technique to obtain three-dimensional information at atomic resolution is the first direct proof of single (dopant) atoms located within the volume of a TEM sample (122) (compare references 4, 119, 120). Volume-rendering techniques can be used to visualize these single atoms in three dimensions. By thresholding intensity values throughout the three-dimensional data set it becomes possible to visualize the location of single atoms in movies with rotating

isosurfaces. A screenshot of the derived model in three dimensions, extracted from the movie, is shown in Figure 22 (see color insert). In this representation, owing to the limited vertical resolution, atoms appear cigar-shaped rather than spherical compared with that seen with the much higher lateral resolution. Note that even columns of Si dumbbells within the Si substrate are visible in the three-dimensional visualization, demonstrating the true three-dimensional character of the acquired data. As can be seen from Figure 22, even some information about interface roughness can be extracted from the recorded data set. However, it should be noted that the depth-slicing method at present does not provide good depth resolution in an aligned crystal because of strong electron channelling effects. Future generations of aberration-corrected microscopes with wider apertures may overcome this limitation (130).

CONCLUDING REMARKS

Throughout this article, we have reviewed the state-of the-art of aberration-corrected scanning transmission microscopy and electron energy loss spectroscopy. We have demonstrated that these techniques can provide new, unique insights into the relations between the structure and the physical properties of a wide variety of heterogeneous systems. The improved sensitivity, both in imaging and spectroscopy, down to the single-atom level has greatly advanced our understanding of catalysts, semiconductors, complex oxides, and many other systems that are of enormous importance to materials science and condensed matter physics today. Furthermore, as we have shown, the basis for the microscopy of the future has been set—a three-dimensional approach to the characterization of solids, nanoscale systems, or interfaces is now possible. It is our belief that the unique role of aberration-corrected STEM (and related techniques) will be pivotal in the development of nanoscience.

ACKNOWLEDGMENTS

We express our most sincere acknowledgment to our collaborators: M. Rühle, S.T. Pantelides, A. Franceschetti, S. Rashkeev, G. Duscher, J. Santamaria, N.D. Browning, S. Overbury, O.L. Krivanek, N. Dellby, P.D. Nellist, L.J. Allen, M.P. Oxley, S.D Findlay, K. Sohlberg, S. Wang, M. Glazov, M. Amiridis, R. Adams, C. Elsaesser, C. Scheu, T. Ochs, U. Alber, D.G. Mandrus, B. Sales, R. Jin, and H.M. Christen. We also want to acknowledge the collaboration of J.T. Luck for TEM specimen preparation and W.H. Sides, Jr. for microscope support. This research was sponsored by the Laboratory for Directed Research and Development Program of ORNL, managed by UT-Batelle, LLC, for the U.S. Department of Energy under Contract No. DE-AC05-00OR22725 and by appointments to the ORNL postdoctoral Research Program administered jointly by ORNL and ORISE and by the Alexander-von-Humboldt Foundation.

Annu. Rev. Mater. Res. 0.0:${article.fPage}-${article.lPage}. Downloaded from arjournals.annualreviews.org
by Oak Ridge National Lab on 06/06/05. For personal use only.

The *Annual Review of Materials Research* is online at http://matsci.annualreviews.org

Annu. Rev. Mater. Res. 0.0:${article.fPage}-${article.lPage}. Downloaded from arjournals.annualreviews.org
by Oak Ridge National Lab on 06/06/05. For personal use only.

LITERATURE CITED

1. Nellist PD, Chisholm MF, Dellby N, Krivanek OL, Murfitt MF, et al. 2004. Direct sub-angstrom imaging of a crystal lattice. *Science* 305:1741
2. Duscher G, Buczko R, Pennycook SJ, Pantelides ST. 2001. Core-hole effects on energy-loss near-edge structure. *Ultramicroscopy* 86:355
3. Rafferty B, Pennycook SJ. 1999. Towards atomic column-by-column spectroscopy. *Ultramicroscopy* 78:141–51
4. Varela M, Findlay SD, Lupini AR, Christen HM, Borisevich AY, et al. 2004. Spectroscopic imaging of single atoms within a bulk solid. *Phys. Rev. Lett.* 92:095502
5. Batson PE, Dellby N, Krivanek OL. 2002. Sub-angstrom resolution using aberration corrected electron optics. *Nature* 418:617–20
6. Wang SW, Borisevich AY, Rashkeev SN, Glazoff MV, Sohlberg K, et al. 2004. Dopants adsorbed as single atoms prevent degradation of catalysts. *Nat. Mater.* 3:143–46
7. Pennycook SJ. 2002. Structure determination through *Z*-contrast microscopy. In *Advances in Imaging and Electron Physics* 123:173–206. San Diego: Academic
8. Pennycook SJ, Nellist PD. 1999. *Z*-contrast scanning transmission electron microscopy. In *Impact of Electron and Scanning Probe Microscopy on Materials Research*, ed. DG Rickerby, U Valdre, G Valdre, pp. 161–207: Amsterdam: Kluwer
9. Nellist PD, Pennycook SJ. 1998. Accurate structure determination from image reconstruction in ADF STEM. *J. Microsc.* 190:159–70
10. Cowley JM. 1969. Image contrast in a transmission scanning electron microscope. *Appl. Phys. Lett.* 15:58
11. Nellist PD, Rodenburg JM. 1994. Beyond the conventional information limit—the relevant coherence function. *Ultramicroscopy* 54:61–74
12. Williams DB, Carter CB. 1996. *Transmission Electron Microscopy*. New York: Plenum
13. Lupini AR, Chisholm MF, van Benthem K, Allen LJ, Oxley MP, et al. 2004. Limitations to the measurement of oxygen concentrations by HRTEM imposed by surface roughness. *Microsc. Microanal.* In press
14. Allen LJ, Findlay SD, Lupini AR, Oxley MP, Pennycook SJ. 2003. Atomic-resolution electron energy loss spectroscopy imaging in aberration corrected scanning transmission electron microscopy. *Phys. Rev. Lett.* 91:105503
15. Lupini AR, Varela M, Borisevich AY, Travaglini SM, Pennycook SJ. 2004. Advances in aberration corrected STEM at ORNL. *Inst. Phys. Conf. Ser.* 179:211–14
16. Lupini AR, Varela M, Borisevich AY, Peng Y, Pennycook SJ. 2003. Prospects for single atom location and identification with aberration-corrected STEM. *Inst. Phys. Conf. Ser.* 180:523–32
17. Lupini AR, Krivanek OL, Dellby N, Nellist PD, Pennycook SJ. 2001. Developments in Cs-corrected STEM. *Inst. Phys. Conf. Ser.* pp. 31–34

17a. Cowley JM. 1979. Adjustment of a STEM instrument by use of shadow images. *Ultramicroscopy* 4:413–18

18. Dellby N, Krivanek OL, Nellist PD, Batson PE, Lupini AR. 2001. Progress in aberration-corrected scanning transmission electron microscop. *J. Electron Microsc.* 50:177–85
19. Scherzer O. 1936. Uber einige Fehler von

Annu. Rev. Mater. Res. 0.0:${article.fPage}-${article.lPage}. Downloaded from arjournals.annualreviews.org
by Oak Ridge National Lab on 06/06/05. For personal use only.

Elektronenlinsen. *Zeit. Phys.* 101:593–603
20. Scherzer O. 1947. Sparische und chromatische Korrektur con Elektronen-Linsen. *Optik* 2:114–32
21. Krivanek OL, Dellby N, Lupini AR. 1999. Towards sub-angstrom electron beams. *Ultramicroscopy* 78:1–11
22. Krivanek OL, Nellist PD, Dellby N, et al. 2003. Towards sub-0.5 angstrom electron beams. *Ultramicroscopy* 96:229–37
23. Rose H. 2004. Outline of an ultracorrector compensating for all primary chromatic and geometrical aberrations of charged-particle lenses. *Nuclear Instr. Method Phys. Res. A* 519:12–27
24. Weissbacker C, Rose H. 2002. Electrostatic correction of the chromatic and of the spherical aberration of charged-particle lenses (Part II). *J. Electron Microsc.* 51:45–51
25. Weissbacker C, Rose H. 2001. Electrostatic correction of the chromatic and of the spherical aberration of charged-particle lenses (Part I). *J. Electron Microsc.* 50:383–90
26. Urban K, Kabius B, Haider M, Rose H. 1999. A way to higher resolution: spherical-aberration correction in a 200 kV transmission electron microscope. *J. Electron Microsc.* 48:821–26
27. Beck V. 1979. A hexapole spherical aberration corrector. *Optik* 53:241–55
28. Crewe AV, Kopf D. 1980. Limitations of sextupole correctors. *Optik* 56:391–99
29. Haider M, Uhlemann S, Schwan E, Rose H, Kabius B, Urban K. 1998. Electron microscopy image enhanced. *Nature* 392:768–69
30. Nellist PD, Pennycook SJ. 1998. Sub-angstrom resolution by underfocused incoherent transmission electron microscopy. *Phys. Rev. Lett.* 81:4156–59
31. Nellist PD, Pennycook SJ. 1999. Incoherent imaging using dynamically scattered coherent electrons. *Ultramicroscopy* 78:111–24
32. Nellist PD, Pennycook SJ. 2000. The principles and interpretation of annular dark-field Z-contrast imaging. *Adv. Imaging Electron Phys.* 113:147–203
33. Kel'man VM, Yavor SY. 1961. Achromatic quadrupole electron lenses. *Sov. Phys. Tech. Phys.* 6:1052–54
34. Deltrap JHM. 1964. *Correction of spherical aberration of electron lenses*. PhD thesis. Univ. Cambridge, Cambridge, UK
35. Satterfield CN. 1980. *Heterogeneous Catalysis in Practice*. New York: McGraw-Hill
36. Wefers K, Misra C. 1987. *Oxides and Hydroxides of Aluminum*. Pittsburgh: Alcoa Labs
37. Church JS, Cant NW, Trimm DL. 1994. Surface-area stability and characterization of a novel sulfate-based alumina modified by rare-earth ions. *Appl. Catal. A* 107:267–76
38. Glazov MV, Novak J, Hector LG. 1999. Stabilization of γ-alumina: how much lanthanum do we actually need? *Alcoa Tech. Pap.* 99:168
39. Kumar KNP, Tranto J, Kumar J, Engell JE. 1996. Pore-structure stability and phase transformation in pure and M-doped (M = La, Ce, Nd, Gd, Cu, Fe) alumina membranes and catalyst supports. *J. Mater. Sci. Lett* 15:266–70
40. Oudet F, Courtine P, Vieux A. 1988. Thermal stabilization of transition alumina by structural coherence with $LaAlO_3$, $PrAlO_3$, $NdAlO_3$. *J. Catal.* 114:112–20
41. Beguin B, Garbowski E, Primet M. 1991. Stabilization of alumina by addition of lanthanum. *J. Catal.* 75:119–32
42. Vazquez A, López T, Gómez R, Morales A, Novaro O. 1997. X-ray diffraction, FTIR, and NMR characterization of sol–gel alumina doped with lanthanum and cerium. *J. Solid State Chem.* 128:161–68
43. Yamamoto T, Tanaka T, Matsuyama T, Funabiki T, Yoshida S. 2001. Structural analysis of La/Al_2O_3 catalysts by La K-edge XAFS. *J. Synchrothron Rad.* 8:634–36
44. Nellist PD, Pennycook SJ. 1996. Direct

Annu. Rev. Mater. Res. 0.0:${article.fPage}-${article.lPage}. Downloaded from arjournals.annualreviews.org
by Oak Ridge National Lab on 06/06/05. For personal use only.

imaging of the atomic configuration of ultradispersed catalysts. *Science* 274:413–15

45. Sohlberg K, Rashkeev S, Borisevich AY, Pennycook SJ, Pantelides ST. 2004. Origin of the anomalous Pt-Pt distances in the Pt/Alumina catalytic system. *Chem. Phys. Chem.* 5:1893–97
46. Valden M, Lai X, Goodman DW. 1998. Onset of catalytic activity of gold clusters on titania with the appearance of nonmetallic properties. *Science* 281:1647–50
47. Haruta M. 1997. Size and support dependency in the catalysis of gold. *Catalysis Today* 36:153–66
48. Bond GC, Thompson DT. 2000. Gold catalyzed oxidation of carbon monoxide. *Gold Bull.* 33:41–51
49. Lupini AR, Franceschetti AG, Pantelides ST, Dai S, Chen B, et al. 2004. Aberration corrected STEM analysis of gold nanoparticle catalytic activity. *Microsc. Microanal*. 10:462–63
50. Hoffmann MJ, Petzow G. 1994. Tailored microstructures of silicon nitride ceramics. *Pure Appl. Chem.* 66:1807–14
51. Lange FF. 1973. Relation between strength, fracture energy, and microstructure of hot-pressed Si_3N_4. *J. Am. Ceram. Soc.* 56:518–22
52. Rühle M, Evans AG. 1989. High toughness ceramics and ceramic composites. *Prog. Mater. Sci.* 33:85–167
53. Hoffmann MJ, Gu H, Cannon RM. 2000. Influence of the interfacial properties on microstructural development and properties of Si_3N_4 ceramics. In *Interfacial Engineering for Optimized Properties II*, ed. CB Carter, EL Hall, CL Briant, S Nutt, pp. 65–74. Warrendale, PA: Mater. Res. Soc.
54. Shibata N, Pennycook SJ, Gosnell TR, Painter GS, Shelton WA, Becher PF. 2004. Observation of rare-earth segregation in silicon nitride ceramics at subnanometre dimensions. *Nature* 428:730–33
55. Wang CM, Pan WQ, Hoffmann MJ, Cannon RM, Rühle M. 1996. Grain boundary films in rare-earth-glass-based silicon nitride. *J. Am. Ceram. Soc.* 79:788–92
56. Kleebe H-J, Rühle M. 1992. Analytical electron microscopy and high-resolution electron microscopy studies of grain-boundary films in silicon nitride-based ceramics. *Mater. Res. Soc. Symp. Proc.* 238:859–64
57. Averill FW, Painter GS. 1994. Symmetrized partial-wave method for density-functional cluster calculations. *Phys. Rev. B* 50:7262–67
58. For more details, visit http://www.pixon.com
59. Painter GS, Becher PF, Shelton WA, Satet RL, Hoffmann MJ. 2004. First-principles study of rare-earth effects on grain growth and microstructure in β-Si_3N_4 ceramics. *Phys. Rev. B* 70:144108
60. Abe E, Yan Y, Pennycook SJ. 2004. Quasicrystals as cluster aggregates. *Nat. Mater.* 3:759–67
61. Abe E, Pennycook SJ, Tsai AP. 2003. Direct atomic-scale observation of a local thermal vibration anomaly in a quasicrystalline $Al_{72}Ni_{20}Co_8$ compound. *Nature* 421:347–50
62. Duscher G, Chisholm MF, Alber U, Ruhle M. 2004. Bismuth-induced embrittlement of copper grain boundaries. *Nat. Mater.* 3:621–26
63. Browning ND, Chisholm MF, Pennycook SJ. 1993. Atomic-resolution chemical analysis using a scanning transmission electron microscope. *Nature* 366:143–46
64. Nakamura K, Kakibayashi H, Kanehori K, Tanaka N. 1997. Position dependence of the visibility of a single gold atom in silicon crystals in HAADF-STEM image simulation. *J. Electron Microsc.* 46:33–43
65. Kohl H, Rose H. 1985. Theory of image-formation by inelastically scattered electrons in the electron microsscope. *Adv. Imaging Electron Phys.* 65:173–227
66. Muller DA, Silcox J. 1995. Delocalization in inelastic-scattering. *Ultramicroscopy* 59:195–213

Annu. Rev. Mater. Res. 0.0:${article.fPage}-${article.lPage}. Downloaded from arjournals.annualreviews.org
by Oak Ridge National Lab on 06/06/05. For personal use only.

67. Holbrook OF, Bird DM. 1995. Theoretical modelling of atomic images formed with inelastically scattered electrons. In *Electron Microscopy and Analysis 1995*, pp. 175–78. Bristol, UK: IOP Publishing
68. Allen LJ, Findlay SD, Oxley MP, Ros souw CJ. 2003. Lattice-resolution contrast from a focused coherent electron probe. Part I. *Ultramicroscopy* 96:47–63
69. Findlay SD, Allen LJ, Oxley MP, Ros souw CJ. 2003. Lattice-resolution contrast from a focused coherent electron probe. Part II. *Ultramicroscopy* 96:65–81
70. Jin S, Tiefel TH, McCormack M, Fastnacht RA, Ramesh R, Chen LH. 1994. Thousandfold change in resistivity in magnetoresistive La-Ca-Mn-O films. *Science* 264:413–15
71. Von Helmolt R, Wecker J, Holzapfel B, Schultz L, Samwer K. 1993. Giant negative magnetoresistance in perovskitelike $La_{2/3}Ba_{1/3}MnO_X$ ferromagnetic films. *Phys. Rev. Lett.* 71:2331–33
72. Dagotto E, Hotta T, Moreo A. 2001. Colossal magnetoresistant materials: the key role of phase separation. *Phys. Rep.* 344:1–153
73. Salamon MB, Jaime M. 2001. The physics of manganites: structure and transport. *Rev. Mod. Phys.* 73:583–628
74. Coey JMD, Viret M, von Molnar S. 1999. Mixed-valence manganites. *Adv. Phys.* 48:167–293
75. Varela M, Franceschetti A, Lupini AR, W. Tian, Jin R, et al. 2005. New insights into charge ordering phenomena in colossal magnetoresistant oxides. *Nature*. Submitted
76. Rask JH, Miner BA, Buseck PR. 1987. Determination of manganese oxidation-states in solids by electron energy loss spectroscopy. *Ultramicroscopy* 21:321–26
77. Leapman RD, Grunes LA, Fejes PL. 1982. Study of the L_{23} edges in the 3D transition-metals and their oxides by electron energy loss spectroscopy with comparisons to theory. *Phys. Rev. B* 26:614–35
78. Krivanek OL, Paterson JH. 1990. ELNES of 3D transition metal oxides. 1. Variations across the periodic table. *Ultramicroscopy* 32:313–18
79. Paterson JH, Krivanek OL. 1990. ELNES of 3D transition metal oxides. 2. Variations with oxidation state and crystal structure. *Ultramicroscopy* 32:319–25
80. Pearson DH, Ahn CC, Fultz B. 1993. White lines and *d*-electron occupancies for the 3D and 4D transition-metals. *Phys. Rev. B* 47:8471–78
81. Vasko VA, Larkin VA, Kraus PA, Nikolaev KR, Grupp DE, et al. 1997. Critical current suppression in a superconductor by injection of spin-polarized carriers from a ferromagnet. *Phys. Rev. Lett.* 78:1134–37
82. Sefrioui Z, Varela M, Peña V, Arias D, Villegas JE, et al. 2002. Superconductivity depression in ultrathin $YBa_2Cu_3O_{7-\delta}$ layers in $La_{0.7}Ca_{0.3}MnO_3$ /$YBa_2Cu_3O_{7-\delta}$ superlattices. *Appl. Phys. Lett.* 81:4568
83. Sefrioui Z, Arias D, Peña V, Villegas JE, Varela M, et al. 2003. Ferromagnetic/superconducting proximity effect in $La_{0.7}Ca_{0.3}MnO_3$/$YBa_2Cu_3O_7$ superlattices. *Phys. Rev. B* 67:214511
84. Peña V, Sefrioui Z, Arias D, Leon C, Santamaria J, et al. 2004. Coupling of superconductors through a half-metallic ferromagnet: evidence for a long-range proximity effect. *Phys. Rev. B* 69:224502
85. Przyslupski P, Komissarov I, Paszkowicz W, Dluzewski P, Minikayev R, Sawicki M. 2004. Magnetic properties of $La_{0.67}Sr_{0.33}MnO_3$/$YBa_2Cu_3O_7$ superlattices. *Phys. Rev. B* 69:134428
86. Holden T, Habermeier HU, Cristiani G, Golnik A, Boris A, et al. 2004. Proximity induced metal-insulator transition in $YBa_2Cu_3O_7$/$La_{2/3}Ca_{1/3}MnO_3$ superlattices. *Phys. Rev. B* 69:064505
87. Varela M, Lupini AR, Pena V, Sefrioui Z, Arslan I, et al. 2005. Direct measurement of charge transfer phenomena at ferromagnetic/superconducting oxide interfaces. *Phys. Rev. Lett.* Submitted

Annu. Rev. Mater. Res. 0.0:${article.fPage}-${article.lPage}. Downloaded from arjournals.annualreviews.org
by Oak Ridge National Lab on 06/06/05. For personal use only.

88. Varela M, Lupini AR, Pennycook SJ, Sefrioui Z, Santamaria J. 2003. Nanoscale analysis of $YBa_2Cu_3O_{7-x}$ /$La_{0.67}Ca_{0.33}MnO_3$ interfaces. *Solid State Electron* 47:2245–48
89. Browning ND, Yuan J, Brown LM. 1992. Determination of the local oxygen stoichiometry in $YBa_2Cu_3O_7$ by electron energy loss spectroscopy in the scanning transmission electron microscope. *Physica C* 202:12–18
90. Browning ND, Chisholm MF, Pennycook SJ, Norton DP, Lowndes DH. 1993. Correlation between hole depletion and atomic-structure at high-angle grain-boundaries in $YBa_2CuO_{7-\delta}$. *Physica C* 212:185–90
91. Henrich VE, Dresselhaus G, Zeiger HJ. 1978. Energy-dependent electron energy loss spectroscopy-application to the surface and bulk electronic structure of MgO. *Phys. Rev. B* 17:4908–21
92. Uchino K. 1994. Ferroelectric ceramics. In *Materials Science and Technology A Comprehensive Treatment—Structure and Properties of Ceramics*, ed. M Swain, RW Cahn, P Haasen, EJ Kramer, 11:635–77. Wenheim, GR: VCH
93. Meixner H, Gerblinger J, Lampe U, Fleischer M. 1995. Thin film gas sensors based on semiconducting metal oxides. *Sensors Actuators B* 23:119–25
94. Setter N, Waser R. 2000. Electroceramic materials. *Acta Mater.* 48:151–78
95. Howe JM. 1993. Bonding, structure and properties of metal-ceramic interfaces. 1. Chemical bonding, chemical reaction and interfacial structure. *Int. Mater. Rev.* 38:233–56
96. Howe JM. 1993. Bonding, structure and properties of metal-ceramic interfaces. 2. Interface fracture-behavior and property measurement. *Int. Mater. Rev.* 38:257–71
97. Finnis MW. 1996. The theory of metal-ceramic interfaces. *J. Phys. Condens. Matt.* 8:5811–36
98. van Benthem K, Elsasser C, Rühle M. 2003. Core-hole effects on the ELNES of absorption edges in $SrTiO_3$. *Ultramicroscopy* 96:509–22
99. van Benthem K, Scheu C, Sigle W, Rühle M. 2002. Electronic structure investigations of Ni and Cr films on (100)$SrTiO_3$ substrates using electron energy-loss spectroscopy. *Z. Metall.* 93:362–71
100. Hohenberg P, Kohn W. 1964. Inhomogeneous electron gas. *Phys. Rev.* 136:B864
101. Kohn W, Sham LJ. 1965. Self-consistent equations including exchange and correlation effects. *Phys. Rev.* 140:A1133
102. van Benthem K, Classen T, Scheu C, Elsasser C, Pennycook SJ, Rühle M. 2005. *Phys. Rev. Lett.* Submitted
103. Kawasaki M, Takahashi K, Maeda T, Tsuchiya R, Shinohara M, et al. 1994. Atomic control of the $SrTiO_3$ crystal surface. *Science* 266:1540–42
104. Polli AD, Wagner T, Rühle M. 1999. Effect of Ca impurities and wet chemical etching on the surface morphology of $SrTiO_3$ substrates. *Surf. Sci.* 429:237–45
105. Ochs T, Kostlmeier S, Elsasser C. 2001. Microscopic structure and bonding at the Pd/$SrTiO_3$ (001) interface—an ab-initio local-density-functional study. *Integr. Ferroelectr.* 32:959–70
106. Ochs T, Elsasser C. 2002. Thin Pd films on $SrTiO_3$ (001) substrates: ab initio local-density-functional theory. *Z. Metall.* 93:406–16
107. van Benthem K, Elsaesser C, Rühle M. 2005. Bonding of thin Pd films on (100)$SrTiO_3$ substrates from density functional theory. *Phys. Rev. B.* Submitted
108. Elsasser C, Takeuchi N, Ho KM, Chan CT, Braun P, Fahnle M. 1990. Relativistic effects on ground state properties of 4d transition metals and 5d transition metals. *J. Physics-Condens. Matter* 2:4371–94
109. Meyer B, Elsaesser C, Lechermann F, Fahnle M. 2003. Fortran 90m program for mixed-basis pseudopotential calculations for crystals. Sttutgart: Max-Planck-Institut fuer Metallforschung
110. van Benthem K, Scheu C, Pennycook SJ,

Annu. Rev. Mater. Res. 0.0:${article.fPage}-${article.lPage}. Downloaded from arjournals.annualreviews.org
by Oak Ridge National Lab on 06/06/05. For personal use only.

Rühle M. 2005. Electronic and atomistic structure investigations of the Pd/$SrTiO_3$ interface using scanning transmission electron microscopy. *Phys. Stat. Sol.* Submitted

111. Bruley J. 1993. Spatially resolved electron energy loss near edge structure analysis of a near Σ11 tilt boundary in sapphire. *Microsc. Microanal. Microstruct.* 4:23
112. Muellejans H, Bruley J. 1995. Electron energy loss near edge structure of internal interfaces by spatial difference spectroscopy. *J. Microsc.* 180:12
113. Scheu C, Stein W, Rühle M. 2000. Electron energy-loss near-edge structure studies of a Cu/(11_20)alpha-Al_2O_3 interface. *Phys. Status Solidi B* 222:199–211
114. Scheu C. 2002. Electron energy-loss near-edge structure studies at the atomic level: reliability of the spatial difference technique. *J. Microsc.* 207:52–57
115. Packan PA. 1999. Perspectives: device physics—pushing the limits. *Science* 285:2079
116. Moore G. 1965. Cramming more components onto integrated circuits. *Electronics* 38:38
117. Tuomi I. 2002. The lives and death of Moore's law. *First Monday*, p. 7
118. van Benthem K. 2005. *Science. Submitted*
119. Lupini AR, Pennycook SJ. 2003. Localization in elastic and inelastic scattering. *Ultramicroscopy* 96:313–22
120. Voyles PM, Muller DA, Grazul JL, Citrin PH, Gossmann HJL. 2002. Atomic-scale imaging of individual dopant atoms and clusters in highly n-type bulk Si. *Nature* 416:826–29
121. Reimer L. 1997. *Transmission Electron Microscopy*. Berlin: Springer
122. van Benthem K. 2005. 3D imaging of individual Hf atoms at a Si/SiO_2/HfO_2 dielectric. *Nature.* Submitted
123. Flannery BP, Deckman HW, Roberge WG, Damico KL. 1987. 3-Dimensional X-ray microtomography. *Science* 237: 1439–44
124. Williams GJ, Pfeifer MA, Vartanyants IA, Robinson IK. 2003. Three-dimensional imaging of microstructure in Au nanocrystals. *Phys. Rev. Lett.* 90:175501
125. Miao J, Ohsuna T, Terasaki O, Hodgson KO, O'Keefe MA. 2002. Atomic resolution three-dimensional electron diffraction microscopy. *Phys. Rev. Lett.* 89:155502
126. de Rosier DJ, Klug A. 1968. Reconstruction of 3D structures from electron micrographs. *Nature* 217:130
127. Midgley PA, Weyland M. 2003. 3D electron microscopy in the physical sciences: the development of *Z*-contrast and EFTEM tomography. *Ultramicroscopy* 96:413–31
128. Koster AJ, Ziese U, Verkleij AJ, Janssen AH, de Jong KP. 2000. Three-dimensional transmission electron microscopy: a novel imaging and characterization technique with nanometer scale resolution for materials science. *J. Phys. Chem. B* 104:9368–70
129. Ritala M, Kukli K, Rahtu A, Raisanen PI, Leskela M, et al. 2000. Atomic layer deposition of oxide thin films with metal alkoxides as oxygen sources. *Science* 288:319–21
130. Peng YP, Nellist PD, Pennycook SJ. 2004. HAADF-STEM imaging with subangstrom probes: a full Bloch wave analysis. *J. Electron Microsc.* 53:257–66

Pennycook.qxd 4/1/05 10:03 PM Page 1

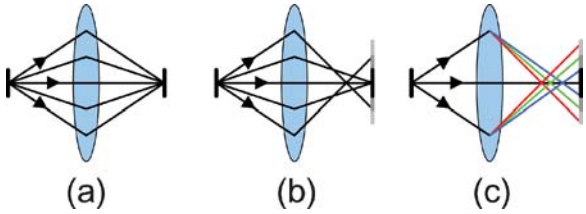

Figure 2 Illustration of the main lens aberrations. (*a*) A perfect lens focuses a point source to a single image point. (*b*) Spherical aberration causes rays at higher angles to be overfocused. (*c*) Chromatic aberration causes rays at different energies (indicated by color) to be focused differently.

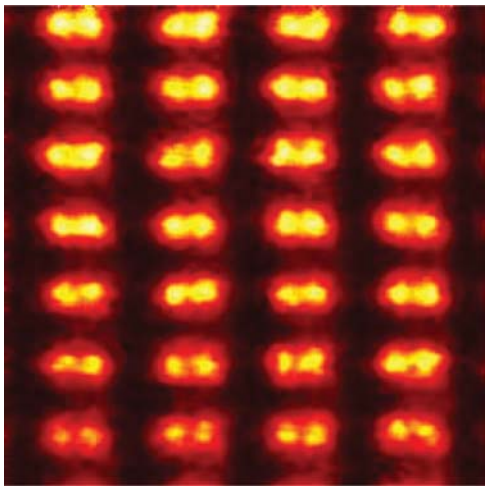

Figure 4 HAADF image of Si [112] recorded with an aberration-corrected STEM. "Dumbbells" just 78 pm apart are resolved.

Annu. Rev. Mater. Res. 0.0:${article.fPage}-${article.lPage}. Downloaded from arjournals.annualreviews.org
by Oak Ridge National Lab on 06/06/05. For personal use only.

Pennycook.qxd 4/1/05 10:03 PM Page 2

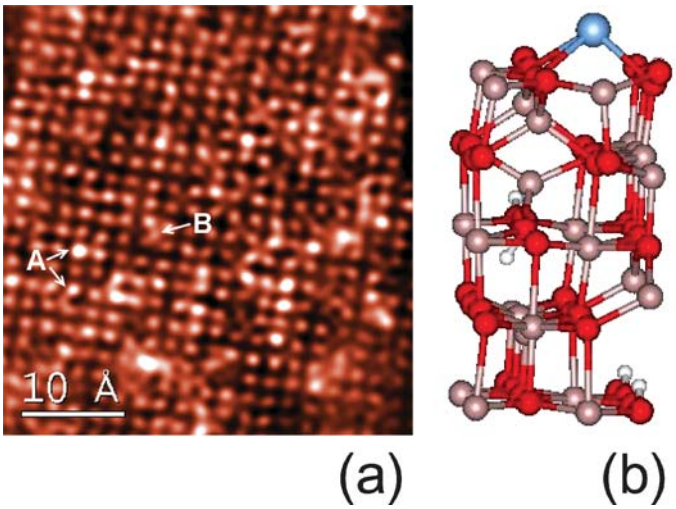

Figure 5 (*a*) *Z*-contrast image of La atoms on γ-Al_2O_3 flake in [100] orientation. Two distinct sites (A and B) for individual La atoms are seen (images are high- and low-pass filtered). (*b*) Schematics of the configuration for the La atom on the (100) surface of γ-Al_2O_3, determined by first-principles calculations.

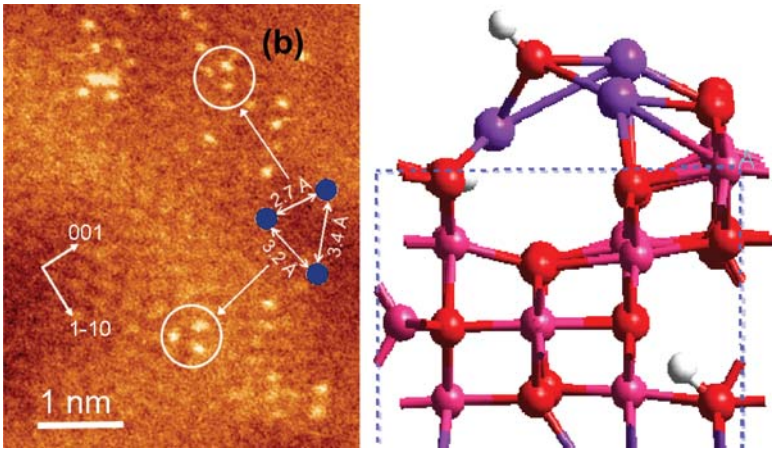

Figure 6 (*a*) *Z*-contrast STEM image of Pt on the surface of γ-Al_2O_3 close to (110) orientation. Two Pt_3 trimer structures are circled; inset, measured interatomic distances. A hint of the underlying alumina lattice is also visible. (*b*) Schematics of the configuration for the Pt_3OH unit on the (110) surface of γ-Al_2O_3, determined by first-principles calculations, with closely matching interatomic distances.

Annu. Rev. Mater. Res. 0.0:${article.fPage}-${article.lPage}. Downloaded from arjournals.annualreviews.org
by Oak Ridge National Lab on 06/06/05. For personal use only.

Pennycook.qxd 4/1/05 10:03 PM Page 3

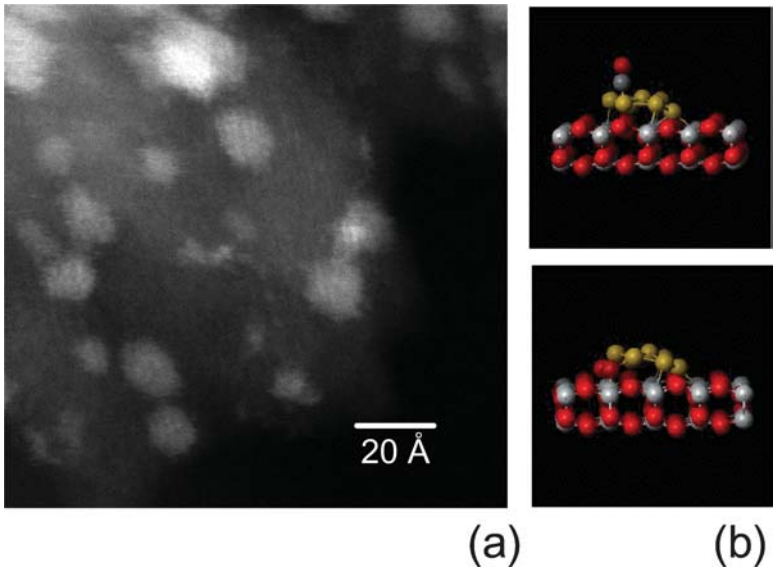

Figure 7 (*a*) *Z*-contrast STEM image showing Au nanoparticles on a titania flake. Most of the nanoparticles are between 1 and 2 nm in diameter and are one to two layers thick. (*b*) First-principles calculations for the observed nanoparticles indicate that they are capable of bonding both CO (*right top*) and O_2 (*right bottom*), shown in the lowest energy configurations, enabling the catalytic activity.

Annu. Rev. Mater. Res. 0.0:${article.fPage}-${article.lPage}. Downloaded from arjournals.annualreviews.org
by Oak Ridge National Lab on 06/06/05. For personal use only.

Pennycook.qxd 4/1/05 10:03 PM Page 4

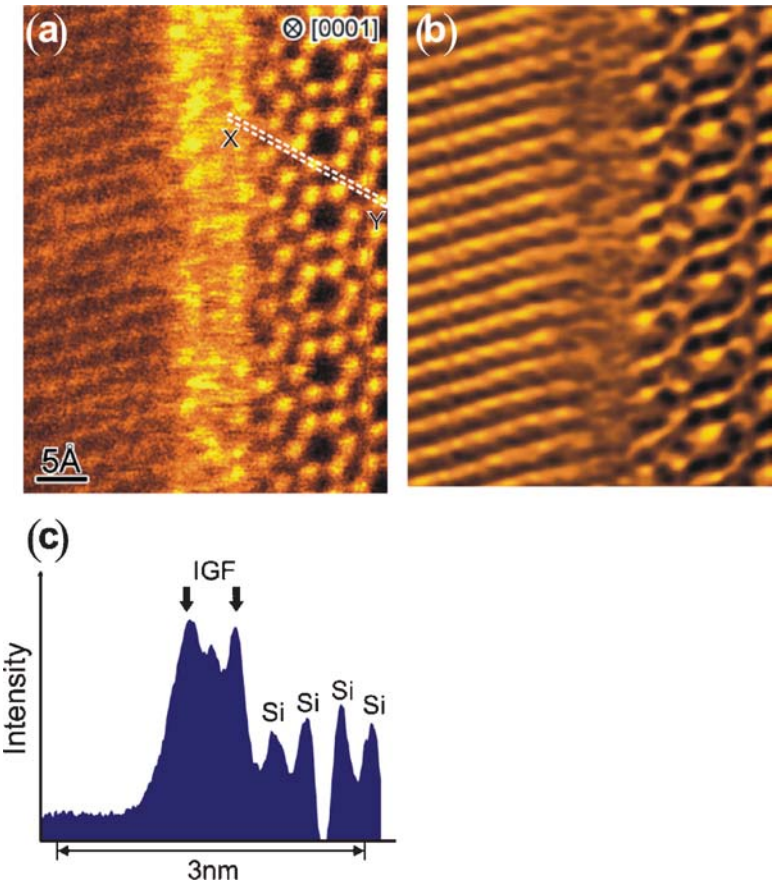

Figure 8 HAADF-STEM (*a*) and bright-field (*b*) STEM images of an intergranular film. (*c*) Intensity line profile taken from the area shown in (*a*).

Annu. Rev. Mater. Res. 0.0:${article.fPage}-${article.lPage}. Downloaded from arjournals.annualreviews.org
by Oak Ridge National Lab on 06/06/05. For personal use only.

Pennycook.qxd 4/1/05 10:03 PM Page 5

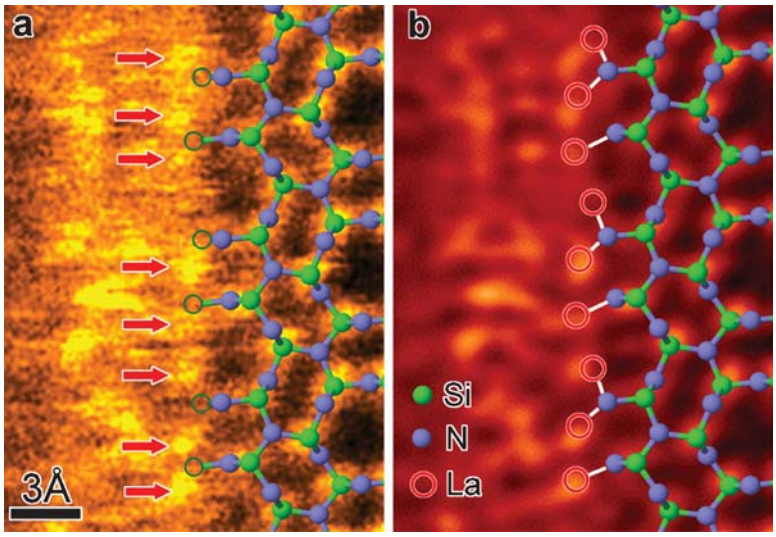

Figure 9 (*a*) Magnified HAADF-STEM image of the IGF/Si_3N_4 interface. A projection view of the β-Si_3N_4 lattice model is superimposed on the image. (*b*) Pixon reconstructed image.

Annu. Rev. Mater. Res. 0.0:${article.fPage}-${article.lPage}. Downloaded from arjournals.annualreviews.org
by Oak Ridge National Lab on 06/06/05. For personal use only.

Pennycook.qxd 4/1/05 10:04 PM Page 6

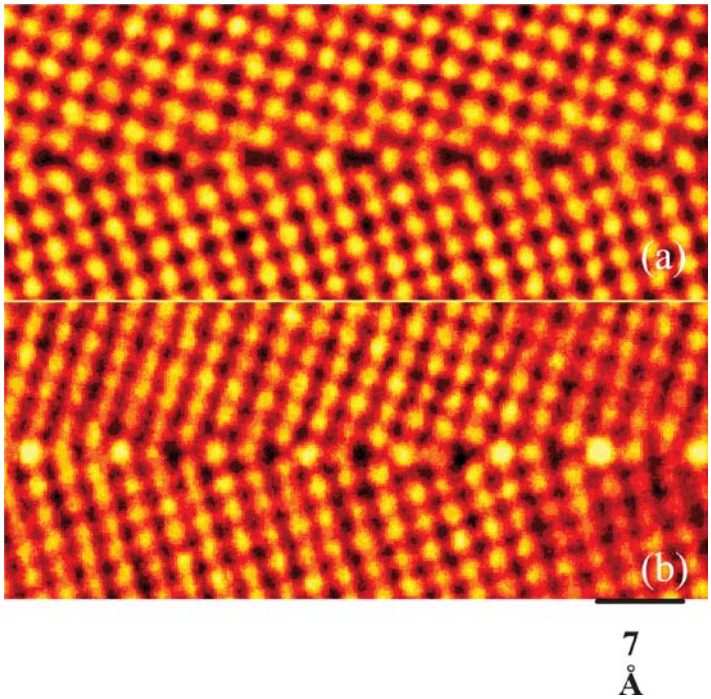

Figure 11 *Z*-contrast images of the grain boundary region of a symmetric 36.8° ⟨001⟩ tilt boundary in (*a*) pure copper and (*b*) bismuth-doped copper. The bismuth segregation site in (*b*) is seen to be distinctly bright [see Duscher et al. (62)].

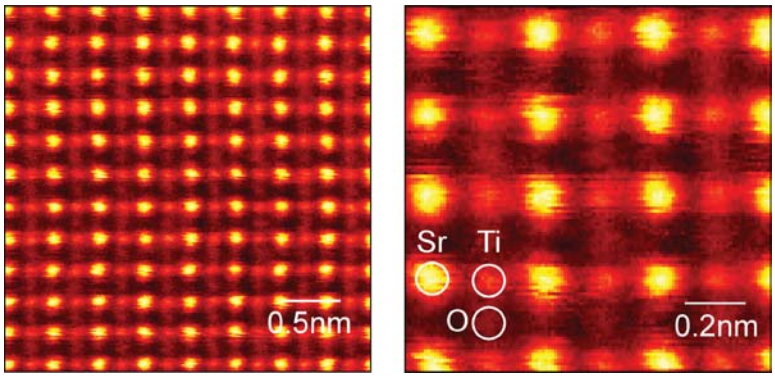

Figure 12 *Z*-contrast images of $SrTiO_3$ viewed down the [011] orientation recorded on the 300 kV aberration-corrected STEM. The oxygen columns are faint, but visible between the Ti columns. No such features are seen between the Sr columns, showing that the faint features are not produced by probe tails.

Annu. Rev. Mater. Res. 0.0:${article.fPage}-${article.lPage}. Downloaded from arjournals.annualreviews.org
by Oak Ridge National Lab on 06/06/05. For personal use only.

Pennycook.qxd 4/1/05 10:04 PM Page 7

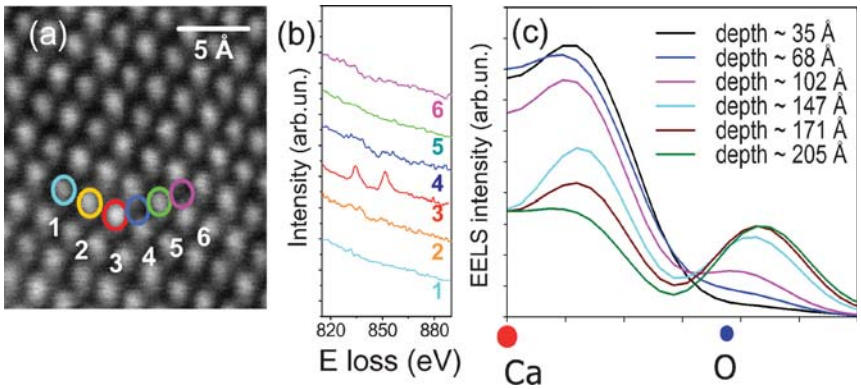

Figure 13 (*a*) HAADF image of a single La atom in a $CaTiO_3$ matrix, acquired in the 100 kV HB501UX STEM. (*b*) Electron energy loss spectra obtained from individual columns of the calcium titanate crystal. The red spectrum reveals the presence of a single La atom within the calcium column circled in red. The signal is substantially reduced from neighboring columns. (*c*) Dynamical simulation of the La spectroscopic image. The ratio of signals on adjacent columns indicates the depth of the atom in the crystal. This atom is approximately 100 Å below the surface.

Annu. Rev. Mater. Res. 0.0:${article.fPage}-${article.lPage}. Downloaded from arjournals.annualreviews.org
by Oak Ridge National Lab on 06/06/05. For personal use only.

Pennycook.qxd 4/1/05 10:04 PM Page 8

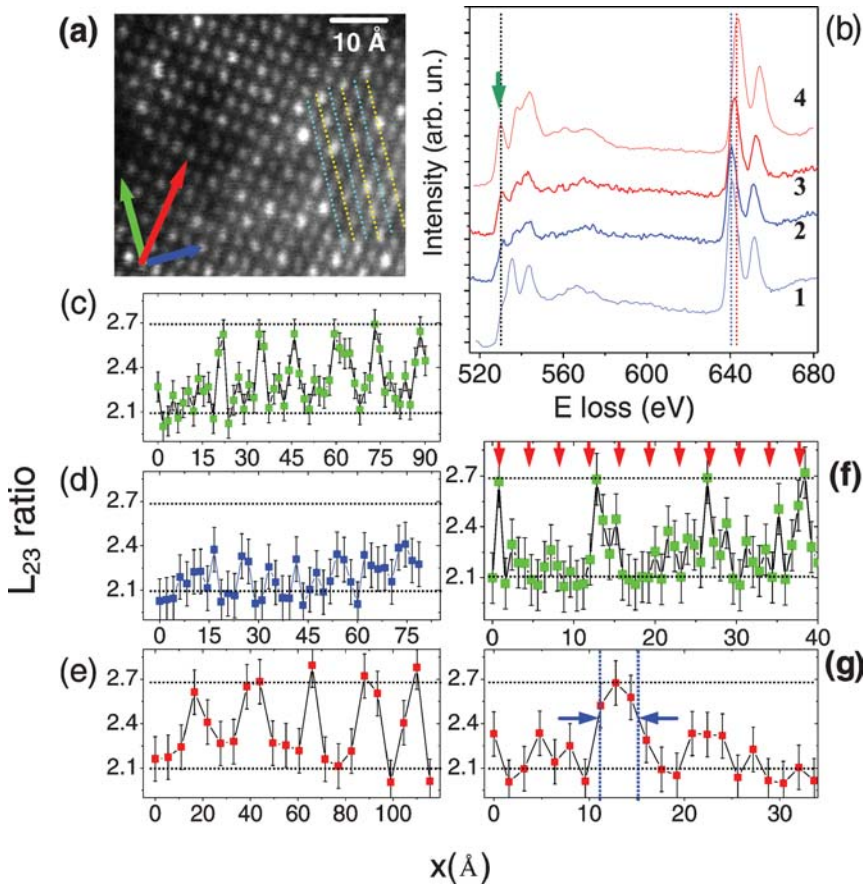

Figure 14 *Z*-contrast image (*a*) and dependence of the L_{23} ratio on position within the BCMO sample for a few specific scan directions. (*b*) Electron energy loss spectra typical of a $Mn^{+3}O$ column (*1*) and a $Mn^{+4}O$ column (*4*). Spectrum (3) comes from $CaMnO_3$, while (4) corresponds to bulk $LaMnO_3$. The oxygen K edge (at 530 eV) and the Mn L edge (around 644 eV) are shown. (*c*) L_{23} ratio along the direction marked with a green arrow in Figure 14*a*. Horizontal lines represent the L_{23} ratio expected for a pure Mn^{+3} oxidation state (*top*) and a pure Mn^{+4} oxidation state (*bottom*). (*d*) L_{23} ratio along the direction marked with a blue arrow in Figure 14*a*. (*e*) L_{23} ratio along the direction marked with a red arrow in Figure 14*a*. Also shown is the dependence of the L_{23} ratio with position in the sample obtained from high magnification EELS linescans: (*f*) scanning along the pseudocubic (100) direction. The positions of Mn planes along the scan have been marked with red arrows. (*g*) Along the pseudocubic (110). Blue arrows mark the estimated width of the stripe, about 4 Å.

Annu. Rev. Mater. Res. 0.0:${article.fPage}-${article.lPage}. Downloaded from arjournals.annualreviews.org
by Oak Ridge National Lab on 06/06/05. For personal use only.

Pennycook.qxd 4/1/05 10:04 PM Page 9

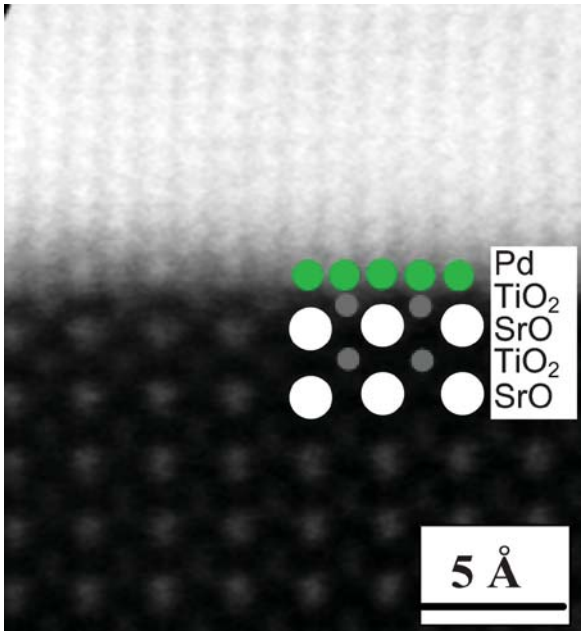

Figure 17 HAADF image of the Pd/$SrTiO_3$ interface recorded in a ⟨100⟩ zone-axis orientation. The intensity line profile clearly reveals Pd atoms sitting on top of oxygen columns of the TiO_2-terminated (100) substrate surface.

Annu. Rev. Mater. Res. 0.0:${article.fPage}-${article.lPage}. Downloaded from arjournals.annualreviews.org
by Oak Ridge National Lab on 06/06/05. For personal use only.

Pennycook.qxd 4/1/05 10:04 PM Page 10

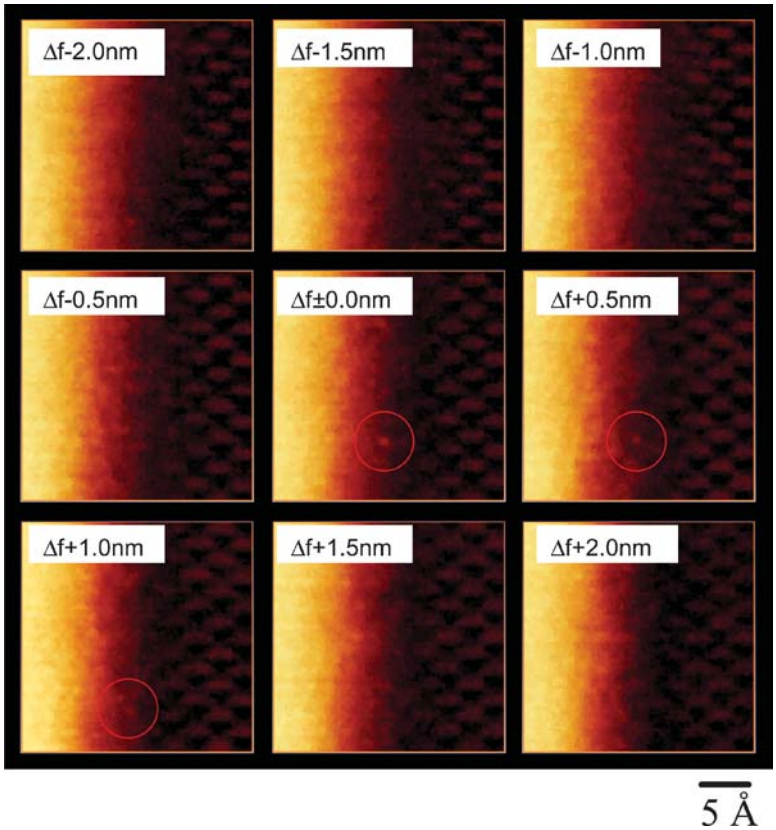

Figure 20 Through-focal-series of a $Si/SiO_2/HfO_2$ interface. The figure shows 9 consecutive micrographs extracted from a series of 21 images recorded at the focal values shown. The focus step size was 0.5 nm between frames. One single Hf atom coming into and going out of focus is marked by a red circle. The micrographs are displayed using a nonlinear contrast scale.

Annu. Rev. Mater. Res. 0.0:${article.fPage}-${article.lPage}. Downloaded from arjournals.annualreviews.org
by Oak Ridge National Lab on 06/06/05. For personal use only.

Pennycook.qxd 4/1/05 10:04 PM Page 11

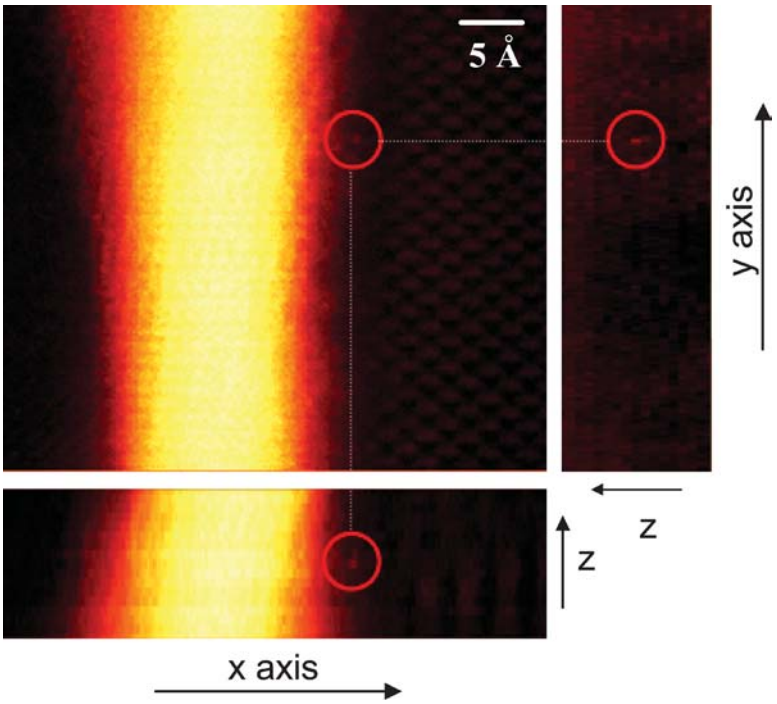

Figure 21 Slice view of the $Si/SiO_2/HfO_2$ interface. The figure shows three different views through the three-dimensional data set. Note that the pixel sizes are about 0.01 nm for the *x* and *y* directions and 0.5 nm in the *z* direction, respectively. The *x*-*y* image shows a single atom in the middle of the SiO_2 interlayer. The *y*-*z* and the *x*-*z* slices clearly show the localization of this single Hf atom in all three dimensions. The *x*-*z* slice even shows columns of the Si dumbbells from the side.

Annu. Rev. Mater. Res. 0.0:${article.fPage}-${article.lPage}. Downloaded from arjournals.annualreviews.org
by Oak Ridge National Lab on 06/06/05. For personal use only.

Pennycook.qxd 4/1/05 10:04 PM Page 12

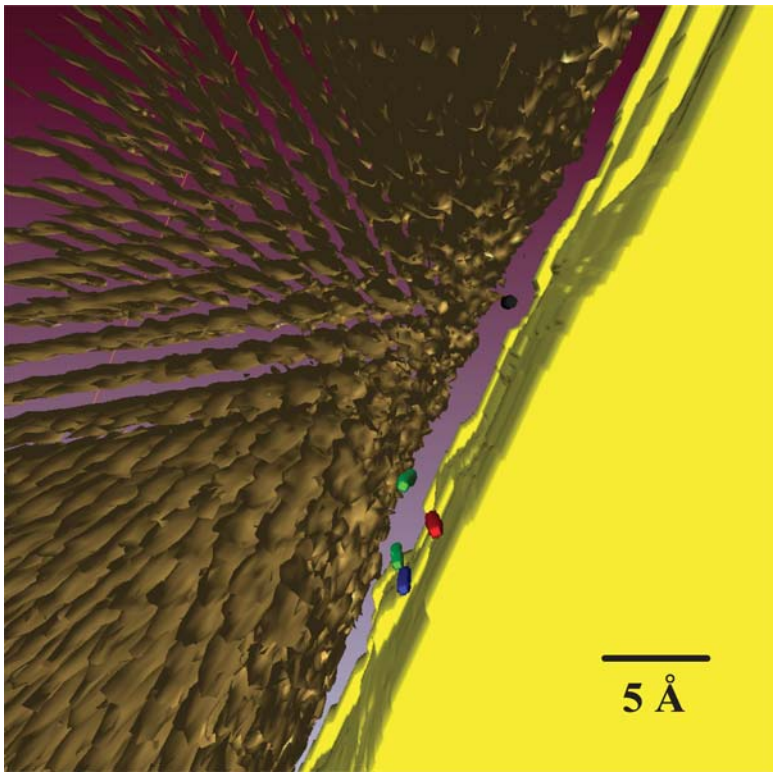

Figure 22 Snapshot of a three-dimensional representation of the $HfO_2/SiO_2/Si$ interface. A three-dimensional representation of the $HfO_2/SiO_2/Si$ interface structure was created by setting thresholds on intensity values from the through-focus-series. The Si substrate was color-coded in gold, whereas the HfO_2 film is marked solid yellow. Single Hf atoms in the interface layer are coded separately in green, black, red, and blue, according to Figures 20 and 21. A movie of the rotating structure can be found in Reference 122. Note that even some surface roughness of the HfO_2 film is observable at the interface with the SiO_2 layer.

Annu. Rev. Mater. Res. 0.0:${article.fPage}-${article.lPage}. Downloaded from arjournals.annualreviews.org
by Oak Ridge National Lab on 06/06/05. For personal use only.